Section 2

Data sets, diagnostic and dynamical investigations, statistical post-processing, reanalysis, and associated studies.

Cyclone and anticyclone activity over the Lake Baikal basin

M.G. Akperov[1], I.I. Mokhov[1,2], M.A. Dembitskaya[1]

[1]A.M. Obukhov Institute of Atmospheric Physics,RAS

[2] Lomonosov Moscow State University

aseid@ifaran.ru

Variations of the hydrological cycle in the Lake Baikal basin are associated with its special geographical location. The catchment basin of Lake Baikal is located in the center of Asia between 46°N and 57°N and between 97°E and 114°E. In recent years, anomalously high values of surface air temperature have been noted with a strong deficit of precipitation in the Lake Baikal basin (Mokhov, Timazhev, 2016b). These extreme climatic phenomena are manifested against the background of the corresponding long-term positive temperature trends and negative precipitation trends for the last decades (http://meteorf.ru/), see also (Climate Change 2014; Obyazov, 2015). The Lake Baikal basin is one of the Russian regions with the strongest warming in summer during the last decades (Groisman et al., 2012). Significant weather-climate anomalies in the Northern Eurasia regions are associated with the El-Nino phenomena (Mokhov, Timazhev, 2016a,b). One of the key factors that play a crucial role in the formation of significant weather and climate anomalies is associated with changes of cyclone and anticyclone activity.

We analyzed seasonal cyclone and anticyclone activities over the Lake Baikal basin (98-112^{o}E) for the two periods (1980-1994 - I and 2002-2016 - II). Cyclone and anticyclone characteristics were calculated from the 6-hourly mean data for sea level pressure from NCEP/NCAR reanalysis. Figure 1 shows the latitudinal distribution of cyclone and anticyclone frequencies (per season) in summer for the different periods.

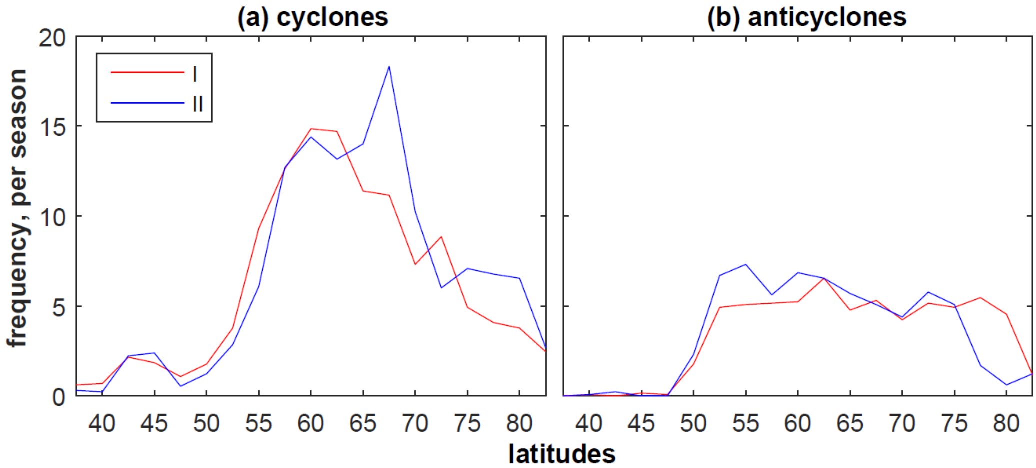

Fig. 1. Latitudinal distribution of cyclone and anticyclone frequencies (per season) in summer for two periods: I – 1980-1994, II – 2002-2016.

The meridional distributions of cyclone and anticyclone frequencies in Figs. 1a,b are very different. The frequency of cyclones in summer shows significant maxima near 60^{o}N for period I and near 70^{o}N for period II. The frequency of summer anticyclones does not show any significant maxima. On the whole, a general decrease in cyclone frequency at lower latitudes (40-60^{o}N) and its general increase at high latitudes (higher than 65 ^{o}N) are found for summer. The changes of opposite sign are noted for the summer anticyclone frequency. Figure 1 shows a general tendency of decreasing the cyclone frequency and increasing the anticyclone frequency over the Lake Baikal basin in summer.

This work was supported by the RFBR and RAS.

References

Climate Change 2014: Impacts, Adaptation, and Vulnerability. Part B: Regional Aspects. Contribution of Working Group II to the Fifth Assessment Report of the Intergovernmental Panel on Climate Change. V.R. Barros et al. (eds.). Cambridge: Cambridge Univ. Press. 2014. 688 p.

Groisman P.Ya., Blyakharchuk T.A., Chernokulsky A.V., Arzhanov M.M., Marchesini L.B., Bogdanova E.G., Borzenkova I.I., Bulygina O.N., Karpenko A.A., Karpenko L.V., Knight R.W., Khov V.Ch., Korovin G.N., Mesherskaya A.V., Mokhov I.I., Parfenova E.I., Razuvaev V.N., Speranskaya N.A., Tchebakova N.M., Vygodskaya N.N. Climate Changes in Siberia. In: Regional Environmental Changes in Siberia and Their Global Consequences (P.Ya. Groisman and G. Gutman eds.). Dordrecht: Springer. 2012, 57-109.

Mokhov I.I., Timazhev A.V. Summer climate anomalies in the Northern Eurasia during intra-annual transitions from El Niño to La Niña. Research Activities in Atmospheric and Oceanic Modelling. E. Astakhova (ed.). 2016a. WCRP Rep. No.15/2016. S. 6. P. 7–8.

Mokhov I.I., Timazhev A.V. Climate anomalies and tendencies of change in Lake Baikal basin // Research Activities in Atmospheric and Oceanic Modelling. E. Astakhova (ed.). 2016b. WCRP Rep. No.15/2016. S. 2. P. 9–10.

Obyazov V.A. Regional response of surface air temperature to global changes: Evidence from the Transbaikal region. Doklady Earth Sci. 2015, **461**(2), 375-378.

TRENDS OF WIND SPEED IN LOW TROPOSPHERE FROM RADIOSONDE DATA OF RUSSIAN ARCTIC STATIONS

O. A. Aldukhov and I. V. Chernykh
Russian Institute of Hydrometeorological Information – World Data Center, Obninsk, Russia,
E-mail: aoa@meteo.ru, civ@meteo.ru

The knowledge about distribution of main meteorological parameters in low troposphere is necessary for many science and practical needs. The paper presents the trends in time series of wind speed (S) in the low troposphere layer from the surface to the 2-km height.

The computations are based on the radiosonde data from eleven Russian Arctic aerological stations located in the North-European, West-Siberian and East-Siberian climatic areas of the Arctic region of Russia. Data from aerological dataset CARDS [1] supplemented by current data from datasets AROCTAB [2] and AROCTAC [3] for the observation period of 1964-2016 were used for this research. The data were subject to a complex quality control procedure. Another quality control procedure was developed especially for the low troposphere layer.

The Akima cubic spline interpolation method was used for calculating S in the atmospheric layer 0–2 km. The trends were estimated using the least squares method.

Table, Figs. 1 and 2 show that the spatiotemporal distribution of the trends is not uniform. The wind speed and standard deviations in the low troposphere layer over the Arctic region of Russia mainly increase at the heights of 400–600 and 400–800 m above the surface, respectively. We can see negative trends near the surface.

The obtained knowledge about long-time changes of wind speed in the low troposphere may be useful for geo-economic justification of nuclear power stations construction, for needs of aviation, shipping, for studying climate change in the Arctic region.

Table. **The ranges of inter-annual changes for the linear trends of anomalies of long-time monthly means and square deviations for wind speed, m/s *decade^{-1}, in the low troposphere layer 0-2-km for 00 and 12 UTC for different climatic areas of the Arctic region of Russia. 1964–2016.**

The ranges of inter-annual changes of the linear trends of anomalies of long-time monthly means S, m/s *decade-1		The ranges of inter-annual changes of the linear trends of anomalies of square deviations for wind speed, m/s *decade-1		Number of observations	
00 UTC	12 UTC	00 UTC	12 UTC	00 UTC	12 UTC
North-European area					
-0,2—<u>**0,7**</u>	-0,4—<u>**0,7**</u>	-0,4—<u>**0,4**</u>	-0,4—<u>**0,4**</u>	58083	56647
West-Siberian area					
-0,6—<u>**0,6**</u>	-0,6—<u>**0,5**</u>	-0,4—<u>**0,3**</u>	**-0,5**—<u>**0,4**</u>	37657	37510
East-Siberian area					
-0,7—<u>**0,8**</u>	-0,5—<u>**0,9**</u>	**-0,5**—***0,4***	**-0,4**—<u>**0,5**</u>	52247	52855

Note. Trends with significance not less than 95% are marked by bold. Trends detected at heights of 400–600 m are underlined and those detected at heights of 700–800 m are shown in italic

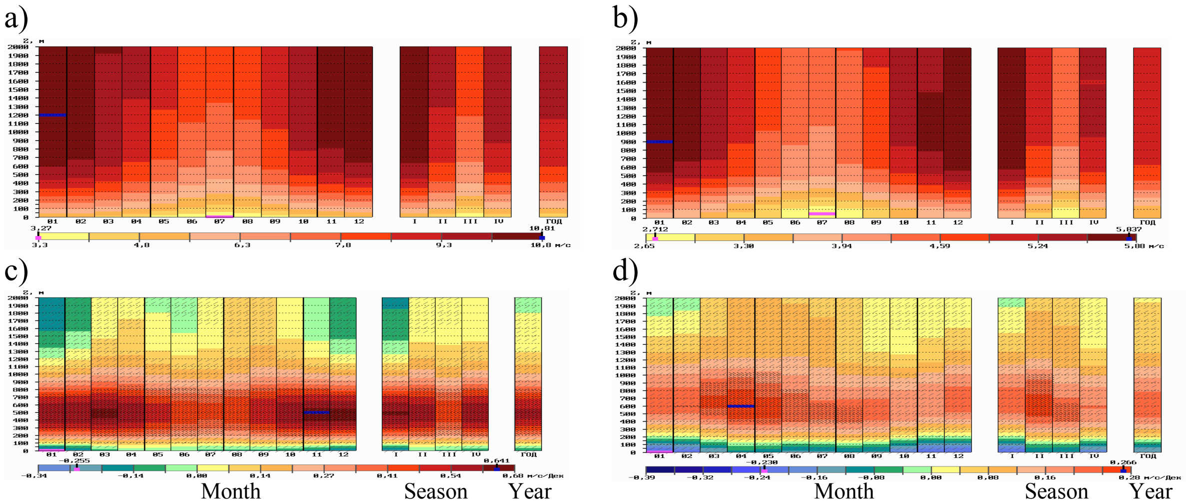

Fig. 1. Long-time mean values (a) and square deviations (b) for wind speed, m/s, the linear trends of anomalies of long-time means (c) and square deviations (d) for wind speed, m/s *decade-1, in the low troposphere layer 0-2-km for 00 UTC for every month, season (I, II, III, IV for DJF, MAM, JJA, SON correspondingly), year. Statistics calculated for station Murmansk for 1964–2016 were smoothed by the twofold smoothing of time series. The three-point smoothing was used. Trends with significance not less than 50% are marked by sloping line segments and trends with significance not less than 95%, by lattice. Blue and pink segments correspond to maximum and minimum values.

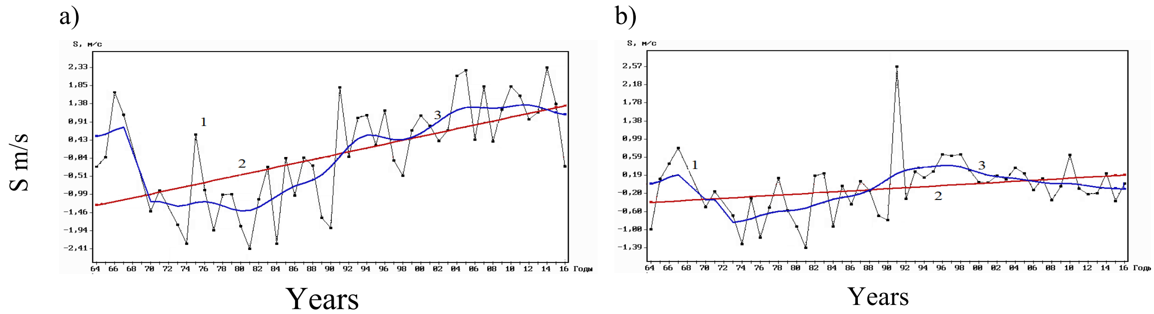

Fig. 2. Black lines (1) – time series for anomalies of means (a) and square deviations (b) for wind speed S, m/s, at height of 500 m for autumn, calculated on the base of upper-air data for station Murmansk for 1964–2016. Red lines (2) show linear trends, blue lines (3) show smoothed trends. The smoothed trends were obtained after the tenfold smoothing of the time series by using the three-point smoothing.

References

1. Eskridge R.E., Alduchov O.A., Chernykh I.V., Zhai P., Polansky A.C., Doty S.R. A comprehensive aerological reference dataset (CARDS): rough and systematic errors // Bull. Amer. Meteor. Soc. 1995. **76.** 1759-1775.
2. Aldukhov O.A. et al. Dataset of current aerological information AROCTAB. Description of the dataset. – Obninsk, RIHMI-WDC, 1990, 28 p.
3. Rudenkova T.V. Format for archiving of the current aerological data, received from GTS for PC // Proc. RIHMI-WDC, 2010, N 174, p. 41—63.

Precipitation type redistribution toward convective rainfall increase over Northern Eurasia in 1965-2017

Chernokulsky A.V., Kozlov F.A.
A.M. Obukhov Institute of Atmospheric Physics RAS, Moscow, Russia
e-mail: a.chernokulsky@ifaran.ru

Precipitation response to the global climate change is not fully investigated yet. It is expected that the frequency of extreme precipitation will increase in a warming climate [1]. In Northern Eurasia, the air temperature and humidity increase results in more frequent formation of convective unstable conditions [2]. It can be expected that warming may redistribute total precipitation toward convective component.

Here, we analyzed different genetic types of precipitation based on routine meteorological observations from 537 Russian stations for the 1966–2017 period [3]. We separated total precipitation into showery (convective), non-showery (stratiform or large-scale) and drizzle precipitation based on information on present and past weather and cloud morphological types (detected and coded during routine observations). We analyzed different characteristics (indices) for precipitation and estimated statistical significance with non-parametric methods.

We found that in Northern Eurasia, the redistribution of precipitation type takes place. In particular, showers become more frequent. In turn, non-showery precipitation becomes less common.

Positive and statistically significant trends are noted at most of the stations for different characteristics of showery precipitation: for seasonal sums (up to 5 mm year^{-1}) (Figs.1a,3), for intensity (not shown) (up to 1-2 mm day^{-1} decade^{-1}) for the 95th percentile (up to 5 mm year^{-1}) (Fig.1b), for the contribution of the 95th percentile into the seasonal sum (up to 7% decade^{-1}) (Fig.2a).

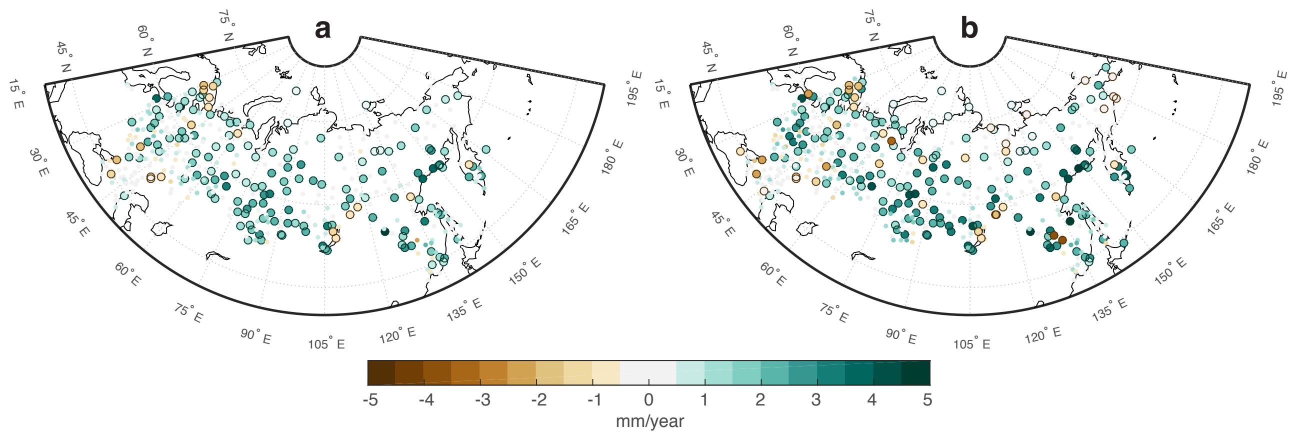

Figure 1. Theil-Sen trends (mm/year) for summer for (a) sum of showery precipitation, (b) the 95th percentile of showery precipitation. Circles stand for each meteorological station (only for stations that located below 500 m height and have less than 5 missed seasons). Large rimmed circles stand for statistically significant trends (at 0.05 significance level based on Mann-Kendall test).

Significant negative trends are noted for the same characteristics for non-showery precipitation (not shown). Opposite trends for showery and non-showery precipitation lead to redistribution between their contributions to the total precipitation (Fig.2b) (drizzle precipitation is negligible). For most of the stations, trends of contribution of convective precipitation are positive, for particular stations they exceed 20% decade^{-1}. As a result, in 1960–1980, non-showery precipitation dominated in Northern Eurasia, while showers have become the predominant type of precipitation in the beginning of the 21st century.

Obtained results can be used for validation of inter-annual variability of convective and large-scale precipitation in global climate models and reanalyses.

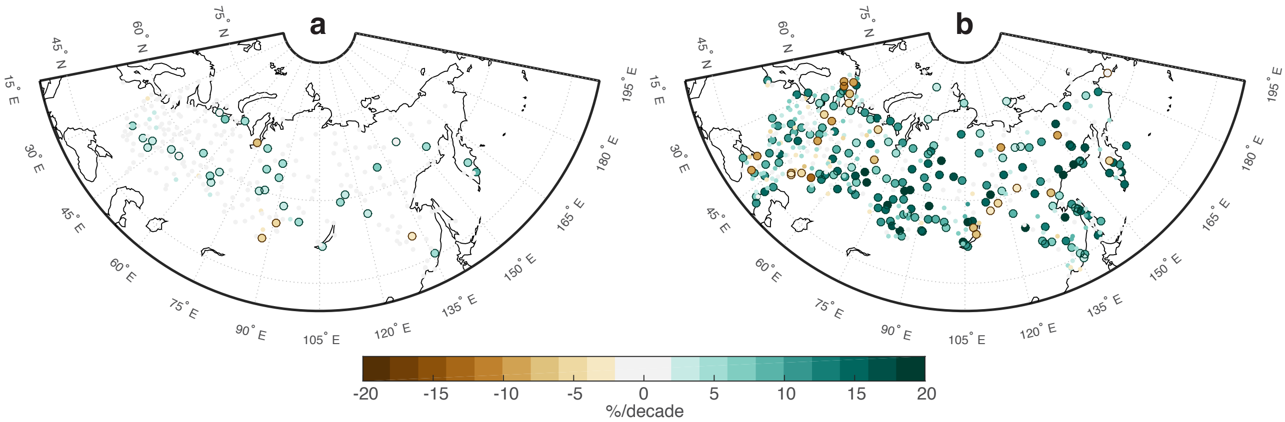

Figure 2. The same as Figure 1, but for (a) contribution of very wet days (95 percentile) to showery precipitation, (b) contribution of showery precipitation to total precipitation.

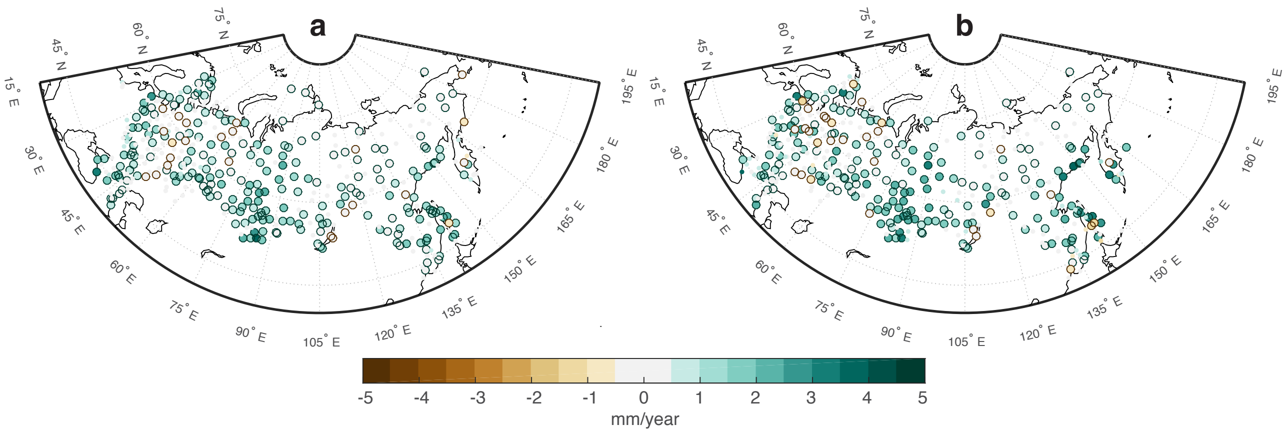

Figure 3. The same as Figure 1, but for sum of showery precipitation in (a) spring and (b) autumn.

The study has been supported by the RFBR project No. 17-29-05098.

References:

1. Meredith E.P., Semenov V.A., Douglas M., Park W., Chernokulsky A.V. Crucial role of Black Sea warming in amplifying the 2012 Krymsk precipitation extreme. // Nature Geosciences, 2015, Vol. 8, P. 615–619.

2. Chernokulsky A.V., Kurgansky M.V., Mokhov I.I. Analysis of Changes in Tornadogenesis Conditions Over Northern Eurasia Based on a Simple Index of Atmospheric Convective Instability // Doklady Earth Sciences. 2017, Vol. 477, Part 2, P. 1504–1509.

3. Chernokulsky A.V., Kozlov F.A., Zolina O.G., Bulygina O.N., Semenov V.A. Climatology of precipitation of different genesis in Northern Eurasia // Russian Meteorology and Hydrology, 2018, Vol. 43, [in press].

Trends in Frequency of Overcast Clouds over the Arctic Region of Russia

I.V. Chernykh and O.A. Aldukhov

Russian Institute of Hydrometeorological Information – World Data Center, Obninsk, Russia,
E-mail: civ@meteo.ru, aoa@meteo.ru

Cloudiness is one of the main components of a climatic system. In this study, the trends of frequency anomalies for cloud layers with clouds covering 80-100% of the sky (the so-called overcast cloud layers) are presented for the Arctic region of Russia. Calculations were conducted for the atmospheric layers 0–2, 2–6, 6–10 km above the surface level for autumn. These layers correspond to low, middle and high-level clouds.

In our research we used the CE-method for cloud boundaries and cloud amount reconstruction [1, 2] and radiosonde sounding data for eleven Arctic Russian stations from dataset CARDS [3] supplemented by current data from datasets AROCTAB [4] and AROCTAC [5] for the 1964-2016 period. The stations are located in the North-European, West-Siberian and East-Siberian climatic areas of the Arctic region of Russia.

The linear trends in the time series of frequency anomalies of the overcast cloud layers were calculated by the least squares method. To compute the trends, only those observations were used that included data both on temperature and on humidity from the surface to the height of 10 km. Together with overcast cloud layers, an existence of cloud layers with other cloud amount was allowable. We did not consider cloud layers for which the CE-method gave thicknesses less than 50 m.

The linear trends of the anomalies of the overcast cloud layers in the atmospheric layers 0-2, 2-6 and 6-10 km are presented for autumn in the Table.

Table

The ranges of changes for the linear trends of anomalies frequency, %*decade^{-1}, of the overcast cloud layers in the atmospheric layers 0-2, 2-6, 6-10 km in autumn for climatic areas of the Arctic region of Russia and the trend significances. 1964–2016.

North-European area		West-Siberian area		East-Siberian area	
Trend, %*decade^{-1}	Significance, %	Trend, %*decade^{-1}	Significance, %	Trend, %*decade^{-1}	Significance, %
6–10 km					
-3,1– -0,1	5–99	-3,9– 0,0	5–99	-1,5–0,5	6–92
2–6 km					
0,4–4,0	31–99	0,1–3,0	4–99	2,7–5,0	99
0–2 km					
3,8–5,1	99	3,0–5,2	96–99	2,3–4,8	98–99

The anomaly time series and their linear trends in autumn are shown in figure for Murmansk and Salekhard for the atmospheric layers considered in the study. Trends obtained after the tenfold smoothing of time series by using the three-point smoothing are also shown.

The presented results demonstrate that the long-time changes of the overcast cloud layers frequency are inhomogeneous in time and space in the atmosphere over the Arctic region of Russia in autumn.

The obtained knowledge about the long-time changes in overcast cloud layers frequency may be useful for studying climate changes in the Arctic region.

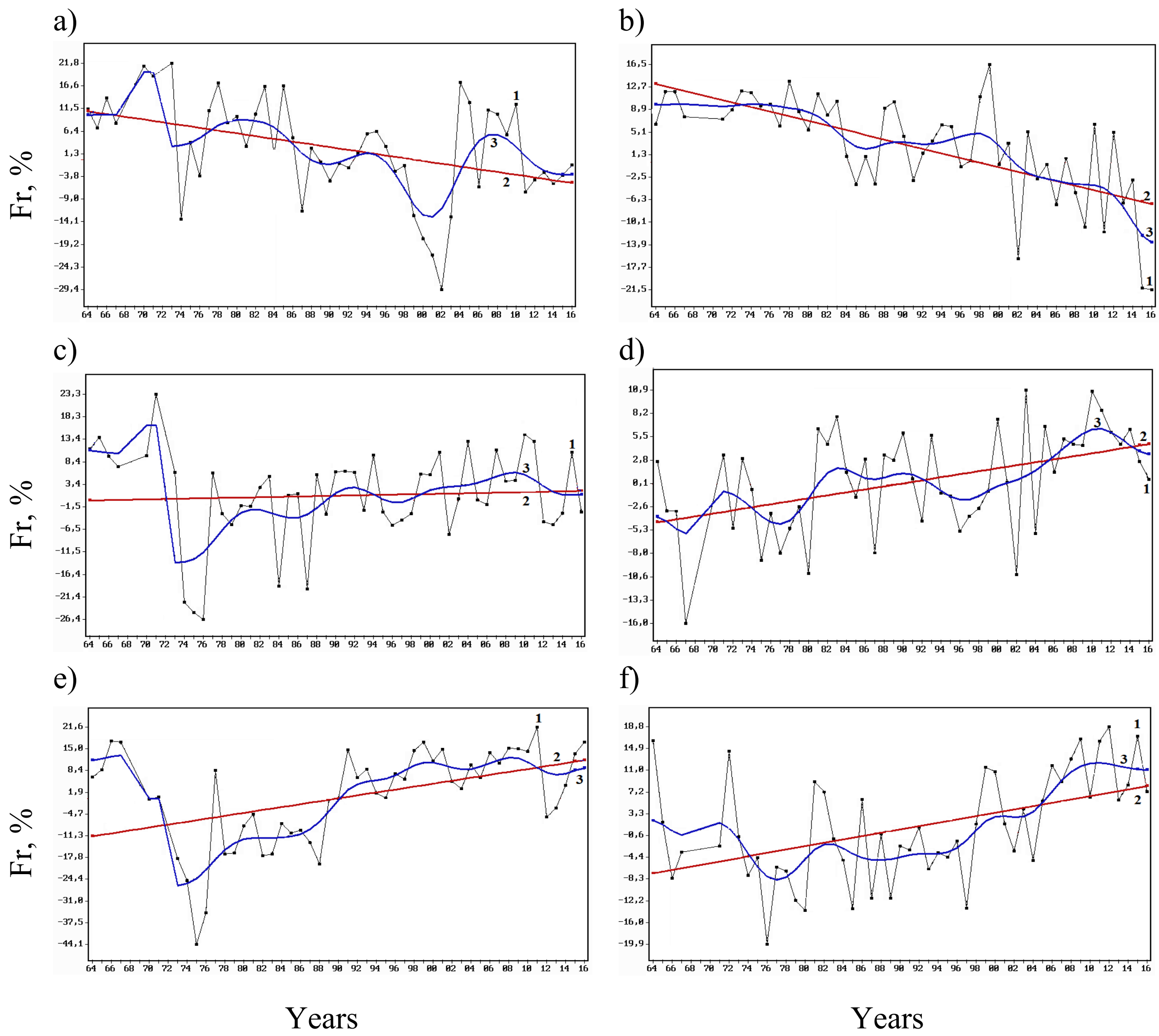

Black lines (1) show the time series for anomalies of frequency of the overcast cloud layers in different atmospheric layers for autumn a), b) layer 6–10 km , c), d) 2–6 km, e), f) 0–2 km, calculated based on the upper-air data for stations Murmansk (a, c, e) and Salekhard (b, d, f) for 1964– 2016. Red lines (2) show linear trends, blue lines (3) show smoothed trends.

References

1. Chernykh I.V. and Eskridge R.E. Determination of cloud amount and level from radiosonde soundings // J. Appl. Meteorol., 1996, vol. 35, pp. 1362—1369.
2. Chernykh I.V., Aldukhov O.A. Vertical distribution of cloud layers from cloud radiosounding data // Izvestiya, Atmospheric and Oceanic Physics. 2004. **40.** No 1. 41-53.
3. Eskridge R.E., Alduchov O.A., Chernykh I.V., Zhai P., Polansky A.C., Doty S.R. A comprehensive aerological reference dataset (CARDS): rough and systematic errors // Bull. Amer. Meteor. Soc. 1995. **76.** 1759-1775.
4. Aldukhov O.A. et al. Dataset of current aerological information AROCTAB. Description of the dataset. – Obninsk, RIHMI-WDC, 1990, 28 p.
5. Rudenkova T.V. Format for archiving of the current aerological data, received from GTS for PC // Proc. RIHMI-WDC, 2010, N 174, p. 41—63.

Trends in global fire occurrence and the role of large-scale atmospheric drivers

Nick Earl and Ian Simmonds

School of Earth Sciences, The University of Melbourne, Victoria 3010, Australia
simmonds@unimelb,edu.au

We are exploring the role of large-scale atmospheric drivers in influencing fire occurrence and variability across the globe. To effect this we are extending the approach we have taken in connection with the variability of fire numbers across the Australian continent (Earl and Simmonds 2017). In particular we are employing the ERA-Interim reanalysis (Dee et al. 2011), and particularly the global atmospheric winds, temperature and humidity.

We are using the 'active fire' (AF) product, giving the location of burning fires, developed by the MODIS Fire Team (June 2000–present), available for download at the NASA Earth Observations website (http://neo. sci.gsfc.nasa.gov/view.php?datasetId=MOD14A1_M_FIRE). The MODIS AF product builds on heritage algorithms for operational fire monitoring used with the Geostationary Operational Environmental Satellites and Advanced Very High Resolution Radiometer sensors, providing information on the specific location of fires, allowing for estimations of emitted energy and the flaming and smouldering ratio. These data have been gridded at 0.1° resolution from the 1 km official MODIS AF product (MOD14A1), which is a level 3 tile-based product from the recently developed MODIS Collection 6. Each pixel assigned to 'fire' has a count of the number of fires within the pixel. We here show the trends and variability of seasonal fire counts over the two hemispheres and the globe.

Figure 1 shows the global distribution of fires that have occurred over the period 2001–2016. Figure 2 exhibits the global and hemispherical fire time series from 2001 to 2016. There is a very strong decline in global fires (statistically significant at $p < 0.001$), present in each season except December–February ($p < 0.1$). The NH is also experiencing a very strong decline ($p < 0.001$) largely resulting from trends in the June–November semester. The SH also displays a strongly significant trend ($p < 0.01$), though not as strong as for the globe or NH. There is much interannual variability across the globe, with 2013 experiencing just 75% of 2001 total. This level of variability is also apparent in both hemispheres.

Similar analyses have been performed for each of the regions indicated in Fig. 1. For further details see Earl and Simmonds (2018).

References

Dee, D. P., et al., 2011: The ERA-Interim reanalysis: Configuration and performance of the data assimilation system. *Quart. J. Roy. Meteor. Soc.*, **137**, 553-597.
Earl, N., and I. Simmonds, 2017: Variability, trends, and drivers of regional fluctuations in Australian fire activity. *J. Geophys. Res.*, **122**, 7445-7460.
Earl, N., and I. Simmonds, 2018: Spatial and temporal variability and trends in 2001-2016 global fire activity. *J. Geophys. Res.*, **123**, 2524-2536.

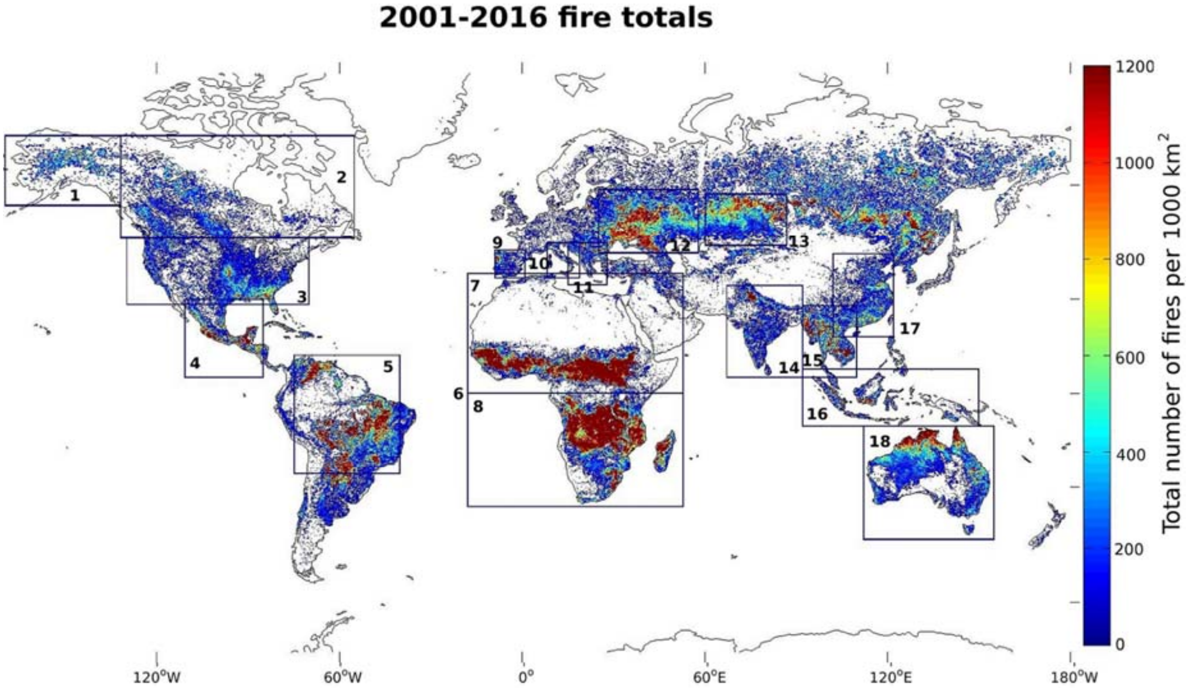

Fig. 1: Total number of annual active fires for the period 2001–2016. The units are fires per 1,000 km^2.

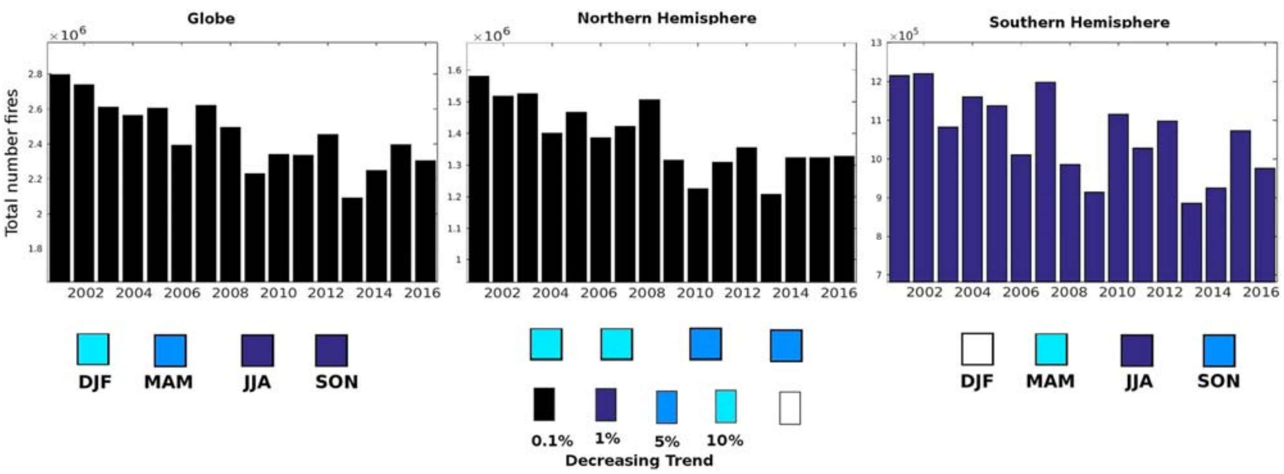

Fig. 2: Global and Hemispherical 2001–2016 fire counts. Levels of significance displayed for the annual trends (colour of bars – decreasing trend: black $p < 0.001$, dark blue $p < 0.01$, middle blue $p < 0.05$, light blue $p < 0.1$) and for each season (represented by the 4 boxes beneath each histogram).

Atmospheric blockings in the Northern Hemisphere: Effects of El Niño and Pacific Decadal Oscillation

Igor I. Mokhov[1,2] and Alexandr V. Timazhev[1]

[1]A.M. Obukhov Institute of Atmospheric Physics RAS
[2]Lomonosov Moscow State University
mokhov@ifaran.ru

Extreme regional hydrometeorological anomalies are related to atmospheric blockings. We analyze here anomalies in blocking activity in the Northern Hemisphere during the last decades in dependence on the key global-scale quasi-cyclic processes like El Niño phenomena and Pacific Decadal Oscillation (PDO, see also (Mokhov et al., 2014; Mokhov, Timazhev, 2014)).

Figure 1 shows the meridional distribution of the atmospheric blocking frequency in the Northern Hemisphere in summer for the period of 1969-2013 for different phases of El Niño phenomena.

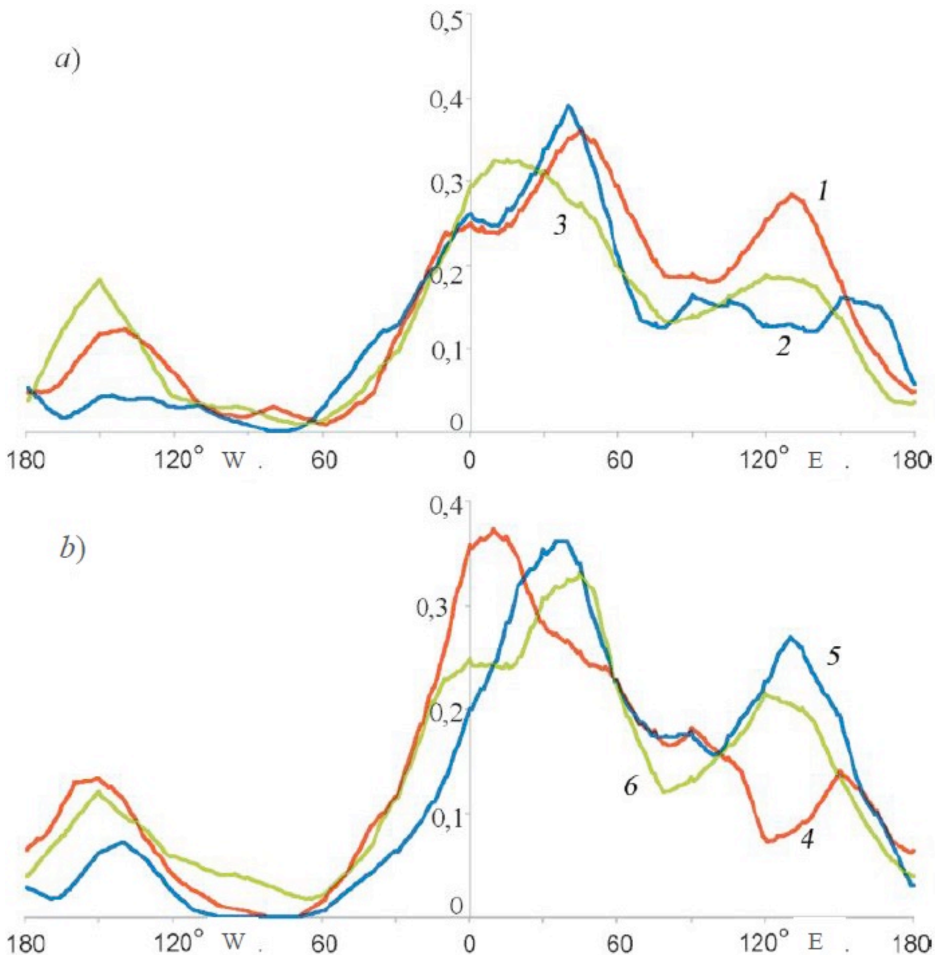

Fig. 1. Meridional distribution of the atmospheric blocking frequency in the Northern Hemisphere in summer for the period of 1969-2013 for different phases of El Niño phenomena: (a) for years with the beginning (a) or ending (b) in the El Niño (La Niña) phase – 1 (4), La Niña phase – 2 (5), or neutral phase – 3 (6).

According to Fig. 1a, the frequency of summer atmospheric blockings in middle latitudes over the eastern part of Asia and western part of the Pacific Ocean is maximum in the years beginning in the El Niño phase and minimal in the years beginning in the phase / La Niña. In this region the frequency of summer blocking is minimal in years ending in the El Niño phase and maximum in years ending in the phase / La Niña (Fig. 1b). Significant variations in the atmospheric blocking frequency in summer for different phases of El Niño / La Niña phenomena occur at mid-latitudes of the eastern part of Northern Eurasia near Lake Baikal and east (see also (Mokhov, Timazhev, 2016)).

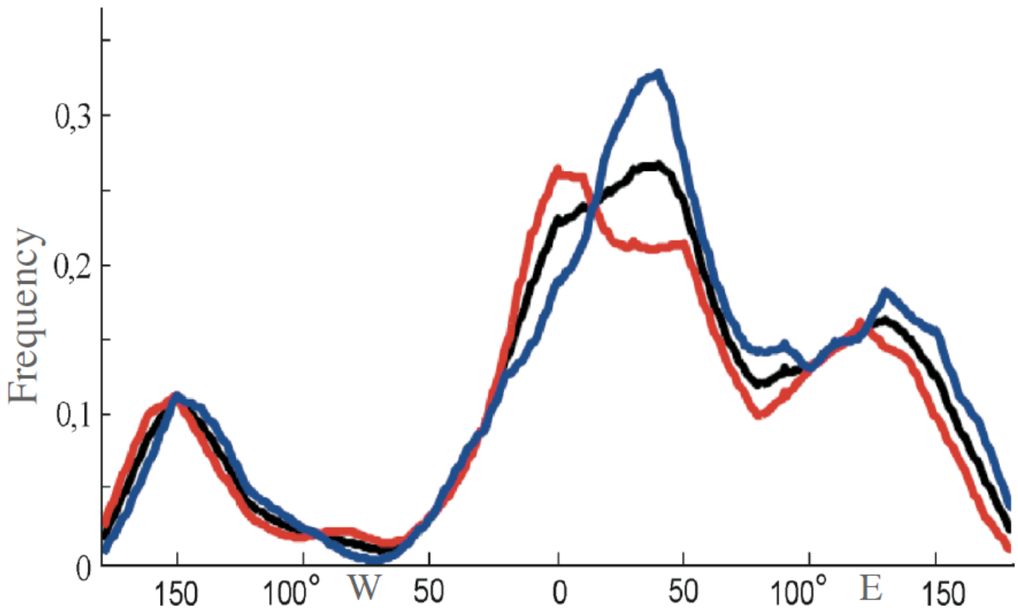

Fig. 2. Mean meridional distribution of the summer blocking frequency in the Northern Hemisphere for the period 1969-2013 (black curve) and separately for the negative (PDO_-, blue curve) and positive (PDO_+, red curve) PDO phase.

Figure 2 shows mean meridional distribution of the summer blocking frequency in the Northern Hemisphere for the period of 1969-2013 and separately for the negative and positive PDO phase. According to Fig. 2, the frequency of summer atmospheric blockings in middle latitudes in the eastern Hemisphere, particularly in Russian regions, is larger in the negative PDO phase than in the positive PDO phase.

This work was supported by the RFBR and RAS.

References

Mokhov I.I., Khon V.C., Timazhev A.V., Chernokulsky A.V., Semenov V.A. Hydrological anomalies and trends in the Amur River basin due to climate changes. In: Extreme Floods in the Amur River Basin: Causes, Forecasts, and Recommendations. Roshydromet, Moscow, 2014, 80-120. (in Russian)

Mokhov I.I., Timazhev A.V. Atmospheric blockings in Northern Hemisphere: variations during last decades. *Research Activities in Atmospheric and Oceanic Modelling.* A. Zadra (ed.), WCRP Rep. № 11/2014. 2014. P.02.09-02.10.

Mokhov I.I., Timazhev A.V. Climate anomalies and tendencies of change in Lake Baikal basin. *Research Activities in Atmospheric and Oceanic Modelling.* E. Astakhova (ed.). 2016. WCRP Rep. No.15/2016. S. 2. P. 9–10.

Atmospheric blockings: Relative frequency of different types

Mokhov I.I.[1,2], Timazhev A.V.[1]

[1]A.M. Obukhov Institute of Atmospheric Physics RAS
[2]Lomonosov Moscow State University
mokhov@ifaran.ru

There are different types of atmospheric blockings, including dipole- or split-type (splitting) blockings (or Rex-type), omega-blockings and meridional blockings (e.g., (Obukhov et al., 1984; Barriopedro et al., 2010)). It should be noted, that splitting blockings can cause long-term change in the mid-latitudinal westerlies to the opposite direction (Mokhov, 2017; Sitnov, Mokhov, 2017; Sitnov et al., 2017). Other types of atmospheric blockings just suppress zonal circulation in the mid-troposhere. We analyze here relative frequency of different types of atmospheric blockings with the use of ERA-Interim reanalysis (Dee et al., 2011).

Dipole-type (split) blockings can be separated from other types of atmospheric blockings as intersections of blocking index areas and 500 hPa zonal wind speed areas on Hovmöller diagram (Figure 1). Figure 1 shows negative Lejenas-Okland blocking index (Lejenas, Okland, 1983) with negative values corresponding to blocking conditions and negative (eastern) zonal wind component at 500 hPa between 40°N and 60°N. The joint realizations of these conditions correspond to split blockings.

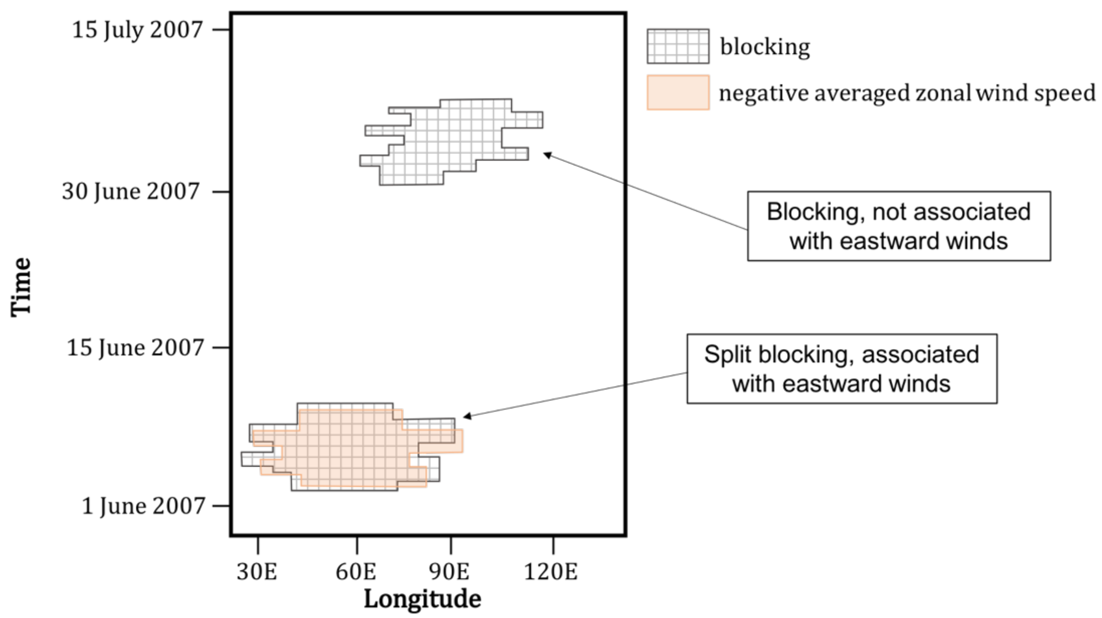

Figure 1. Hovmöller diagram for Lejenas-Okland blocking index and for zonal wind component at 500 hPa between 40°N and 60°N.

Figure 2 shows variations of relative contribution of dipole-type (split) blockings to the total number of blockings and total duration of blockings in the Northern Hemisphere in summer (red color) and winter (blue color) during the period 1979-2016. Corresponding dotted lines characterize linear trends for winter for the total period (1979-2016) and for summer for two sub-periods (1979-2000, 2001-2016).

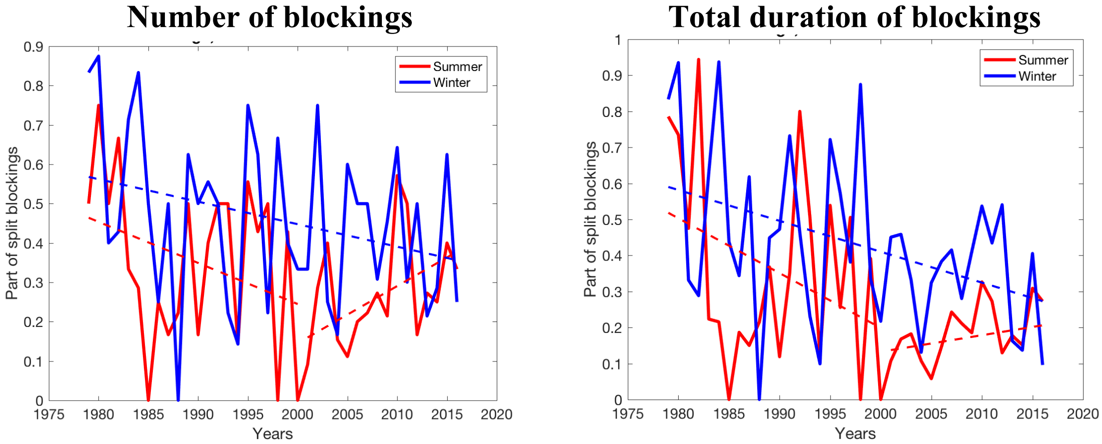

Figure 2. Variations of relative contribution of dipole-type (split) blockings to the total number of blockings and total duration of blockings in the Northern Hemisphere in summer (red color) and winter (blue color) during the period 1979-2016. Corresponding dotted lines characterize linear trends for winter for the total period (1979-2016) and for summer for two sub-periods (1979-2000, 2001-2016).

According to Fig. 2 there is a general tendency of decrease for relative contribution of split blockings to the total blockings number and duration. At the same time, it should be noted that in recent years there has been a growing tendency for the relative role of splitting blockings, particularly for the period 2001-2016 in the summer.

This work was supported by the RFBR and RAS.

References

Barriopedro D., García-Herrera R., Trigo R.M. Application of blocking diagnosis methods to general circulation models. Part I: a novel detection scheme. *Climate Dynamics*. 2010, **35**, 1393–1409.

Dee D.P. et al. The ERA-Interim reanalysis: configuration and performance of the data assimilation system. *Q. J. R. Meteorol. Soc.* 2011, **137**, 553–597.

Lejenas H., Okland H. Characteristics of Northern Hemisphere blocking as determined from a longtime series of observational data. *Tellus A.* 1983, **35**, 350-362.

Mokhov I.I. Atmospheric blockings and related climatic anomalies. In: Nonlinear Waves' 2016. Nizhny Novgorod, IAP RAS, 2017, 111-124 (in Russian).

Obukhov A.M., Kurgansky M.V., Tatarskaya M.S. (1984) Dynamical conditions for the origin of droughts and other large-scale weather anomalies. *Meteorol. Hydrol.,* 1984, **10**, 5-13.

Sitnov S.A., Mokhov I.I. Anomalous transboundary transport of the products of biomass burning from North American wildfires to Northern Eurasia. *Doklady Earth Sci.*, 2017, **475**(1), 832–835.

Sitnov S.A., Mokhov I.I., Gorchakov G.I. The link between smoke blanketing of European Russia in summer 2016, Siberian wildfires and anomalies of large-scale atmospheric circulation. *Doklady Earth Sci.*, 2017, **472**(2), 190–195.

Link of the Barents Sea ice extent with El-Nino phenomena

I.I. Mokhov[1,2] and M.R. Parfenova[1]

[1]A.M. Obukhov Institute of Atmospheric Physics RAS
[2]Lomonosov Moscow State University
mokhov@ifaran.ru

The most rapid current climate changes are detected in the Arctic. One of the brightest proofs of the current changes is the rapid reduction of the Arctic sea ice extent (Mokhov, 2015). The strongest interannual variations of the global climate are associated with El-Niño phenomena and it is natural to expect the manifestation of El-Niño effects in different latitudes, especially in Arctic latitudes. An important indicator of changes in the Arctic basin is the Barents Sea (Mokhov, 2018). It is a key reservoir of heat accumulated in the Arctic Ocean. At the same time, climatic conditions in the Barents Sea basin are sensitive to possible variations in oceanic thermohaline circulation, which is formed in the North Atlantic and is dependent on the global climate. A number of studies have noted a relationship between climatic variations in the Barents Sea basin and El-Niño phenomena (see (Byshev, 2003)). Here we analyze the changes in the features of the connection between the Barents Sea ice extent (BSIE) by data from (http://nsidc.org) with El-Niño phenomena (EN) of various types characterized by different indices.

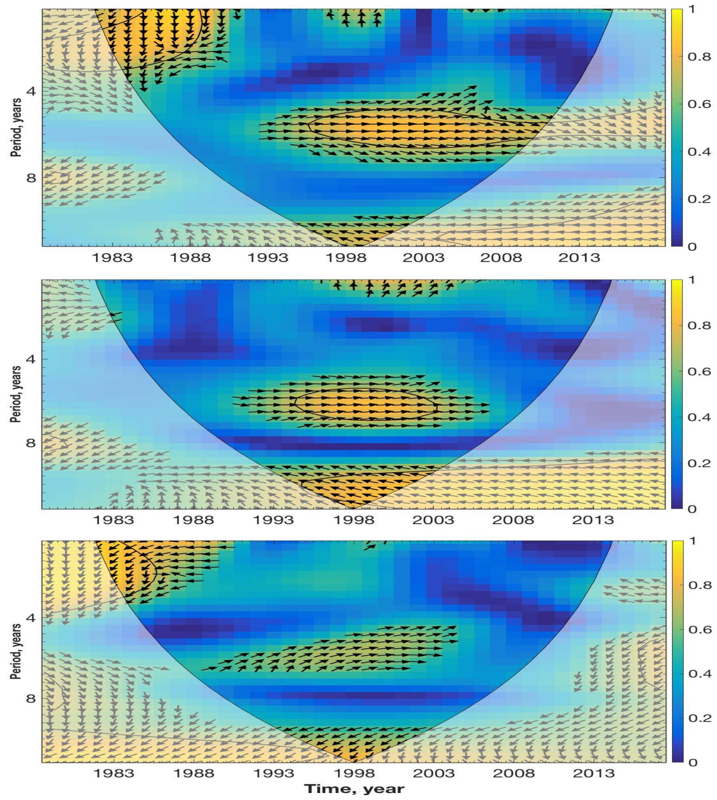

a

b

c

Fig. 1. Local coherence of BSIE in February (a), April (b) and September (c) with EN (Nino3) in January from observations (1979-2018).

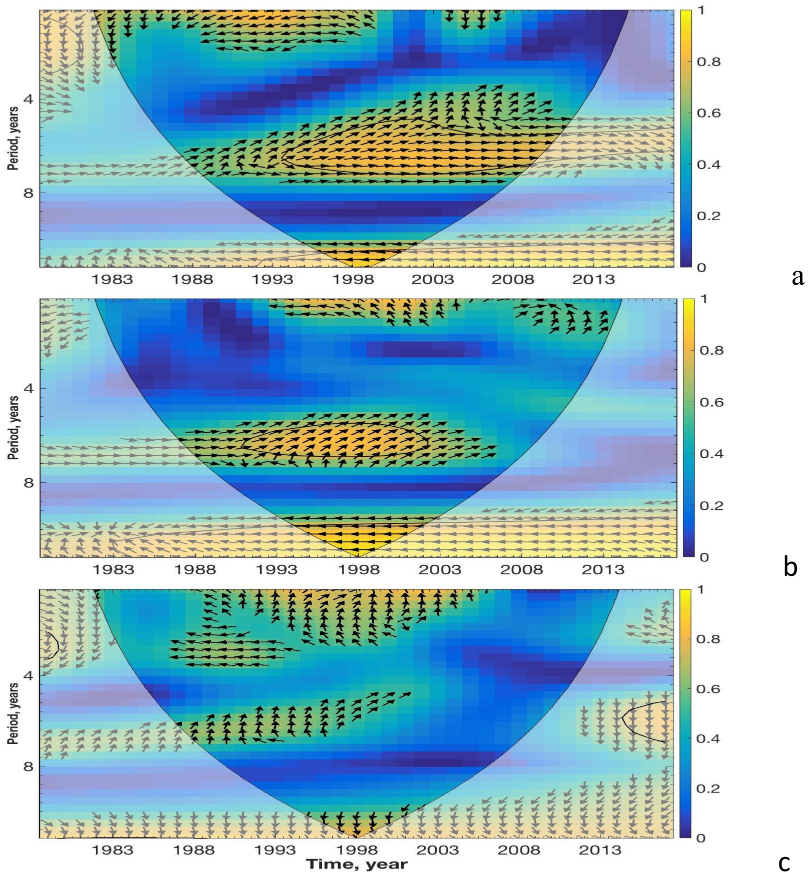

Fig. 2. Local coherence of BSIE in February (a), April (b) and September (c) with EN (Nino4) in January from observations (1979-2018).

Figures 1,2 show local coherence of BSIE in February (a), April (b) and September (c) with EN characterized by Nino3 and Nino4 indices in January from observations (1979-2018). The significant BSIE-EN coherence is exhibited for variations with periods about 5-6 years and for interdecadal (long-term) variability. It should be also noted the manifestation of the relationship of Barents Oscillation to the El Niño phenomena.

There are remarkable differences for different months. In particular, the BSIE-EN coherence is more significant in February and April (with a large BSIE in winter and spring months) than in September (with BSIE intra-annual minimum at the end of summer - beginning of fall). Figures 1, 2 display essential differences in the BSIE coherence with different EN types detected by Nino3 and Nino4, especially in the interdecadal variability. According to Fig. 1 the long-term BSIE coherence with EN (Nino3) is insignificant in September during two first decades of the 21st century while it was significant during last two decades of the 20th century. The obtained results can be explained by the existence of a critical BSIE value below which its relationship with EN becomes statistically insignificant.

This work was supported by the RFBR and RAS.

References

Byshev V.I. Synoptical and Large-Scale Variability of Ocean and the Atmosphere. Moscow, Nauka, 2003, 343 pp. (in Russian)

Mokhov I.I. Contemporary climate changes in the Arctic. *Herald Russ. Acad. Sci.,* 2015, **85** (3), 265–271.

Mokhov I.I. Assessment of the ability of contemporary climate models to assess adequately the risk of possible regional anomalies and trends. *Doklady Earth Sci*., 2018, **479** (2), 482–485.

Relationship between the Caspian Sea level and the Arctic sea ice extent

I.I. Mokhov[1,2] and M.R. Parfenova[1]

[1]A.M. Obukhov Institute of Atmospheric Physics RAS
[2]Lomonosov Moscow State University
mokhov@ifaran.ru

One of the largest regional climate variations during the last century is associated with hydrological cycle variations in the Caspian Sea basin with a large anomalies of the Caspian Sea level (CSL) (Arpe et al., 1999; Arpe et al., 2000). Enclosed seas and large lakes like Caspian Sea are sensitive indicators of the global climate and water balance changes (Mokhov, Khon, 2001). The most significant current climate changes are detected in the Arctic with the rapid reduction of the Arctic sea ice extent (Mokhov, 2015). Influence of the strongest changes in the Arctic should be manifested in the middle latitudes, in particular in regions sensitive to global changes. We analyze here the relationship of CSL with the Arctic ice extent. This connection has been studied for a long time, since the days of L. Berg and W. Wiese. We estimate changes in the relationship of CSL with the Arctic ice extent from observations during last decades with the use of cross-wavelet analysis.

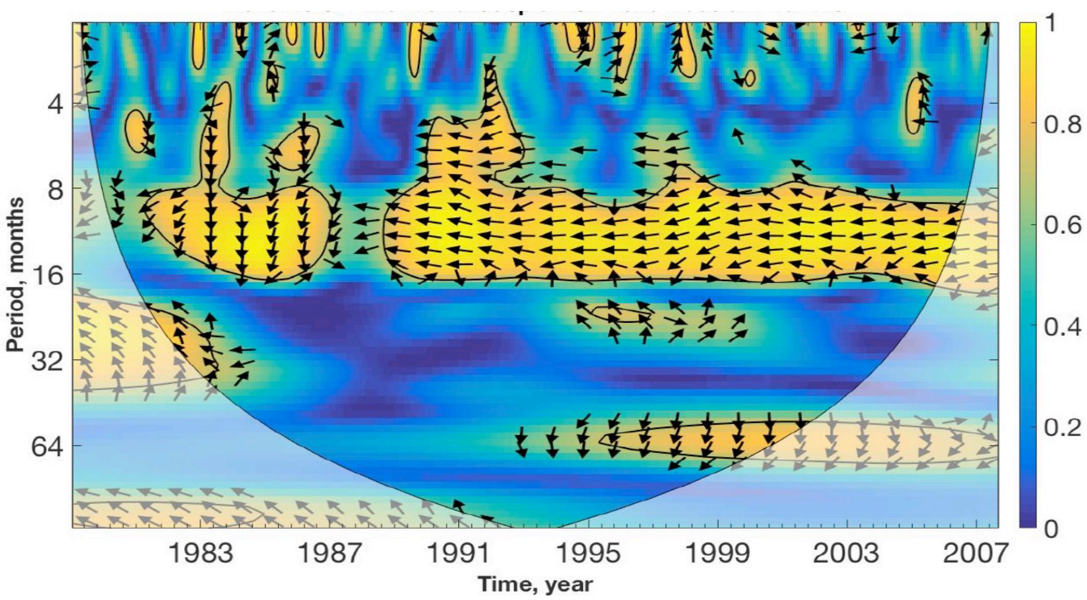

Fig. 1. Local coherence of CSL with BSIE by monthly-mean data for the period 1979-2008.

Figures 1,2 show local coherence of CSL (at Makhachkala) with the Barents Sea ice extent (BSIE) and Kara Sea ice extent (KSIE) by monthly-mean data from (http://nsidc.org) for the period 1979-2008. Along with significant coherence for variations in the annual cycle, significant coherence is exhibited for CSL with BSIE and KSIE variations with periods about 5 years and for interdecadal (long-term) variability. The coherence of CSL with variations of BSIE and KSIE with periods of about 5 years (characteristic for El Niño phenomena) was manifested only in last years.

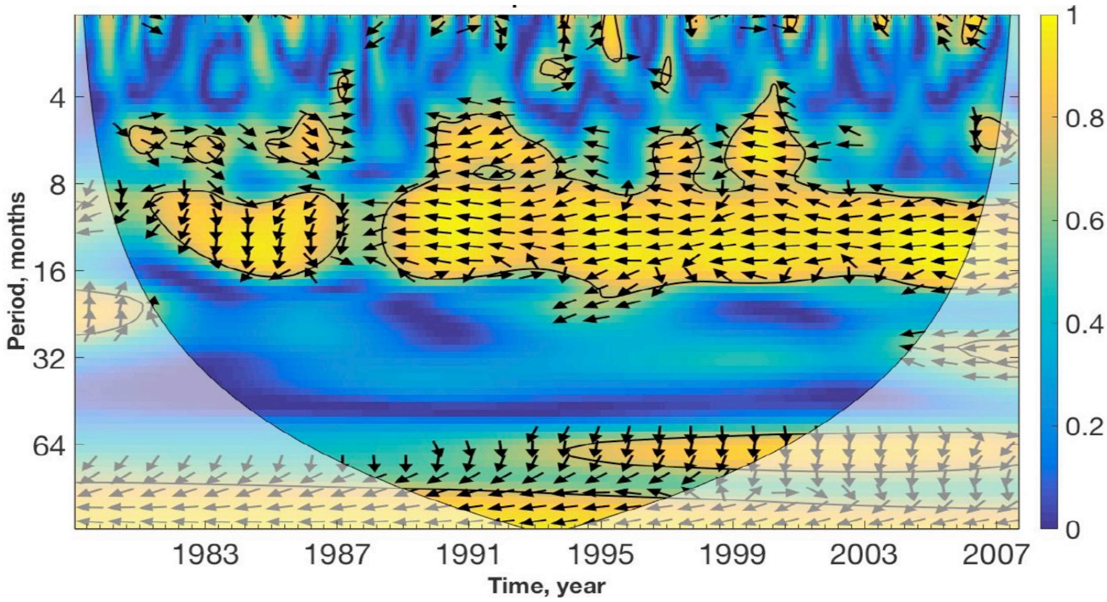

Fig. 2. Local coherence of CSL with KSIE by monthly-mean data for the period 1979-2008.

Interdecadal (long-term) CSL and sea ice extent coherence is more significant for KSIE than for BSIE (Fig. 2). According to Fig. 1, the coherence of CSL with BSIE in the interdecadal variability became statistically insignificant from the end of the 20th century.

This work was supported by the RFBR and RAS.

References

Arpe K., L. Bengtsson, Golitsyn G.S., Mokhov I.I., Semenov V.A., Sporyshev P.V. Analysis and modelling of the hydrological regime variations in the Caspian Sea basin. *Doklady Earth Sci.*, 1999, **366**, 552-556.

Arpe K., L. Bengtsson, Golitsyn G.S., Mokhov I.I., Semenov V.A., Sporyshev P.V. Connection between Caspian Sea level variability and ENSO. *Geophys. Res. Lett.*, 2000, **27**, 2693-2696.

Mokhov I.I. Contemporary climate changes in the Arctic. *Herald Russ. Acad. Sci.,* 2015, **85**(3), 265–271.

Mokhov I.I., Khon V.Ch. Projections of future changes of hydrological cycle in the Caspian Sea basin. *Res. Activ. Atmos. Ocean. Modell.* Ed. by H. Ritchie. WMO/TD-No. 1064. 2001, 9.20-9.21.

Squalls with a hurricane wind in Moscow

Mokhov I.I.[1,2], Timazhev A.V.[2], Yushkov V.P.[1]

[1]Lomonosov Moscow State University
[2]A.M. Obukhov Institute of Atmospheric Physics RAS

mokhov@ifaran.ru
yushkov@phys.msu.ru

The results of measurements of wind speed by an ultrasonic anemometer (50 Hz) during the strongest squalls in Moscow on 29 May, 2017 and 21 April, 2018 at the Physics Faculty of the Lomonosov Moscow State University (PF MSU) on the Vorob'evy (Leninskie) Gory (55°42'00.28" N, 37°31'45.30" E) at an altitude of 50 m above the surface are analyzed.

Figure 1 shows variations of the zonally (U) and meridionally (V) oriented components of the wind, as well as the vertical velocity (W) components during 3 hours (14-17) on 29.05.2017 from measurements at PF MSU. The strongest squall with a wind of hurricane strength (more than 32 m/s) was registrated at 15:39.

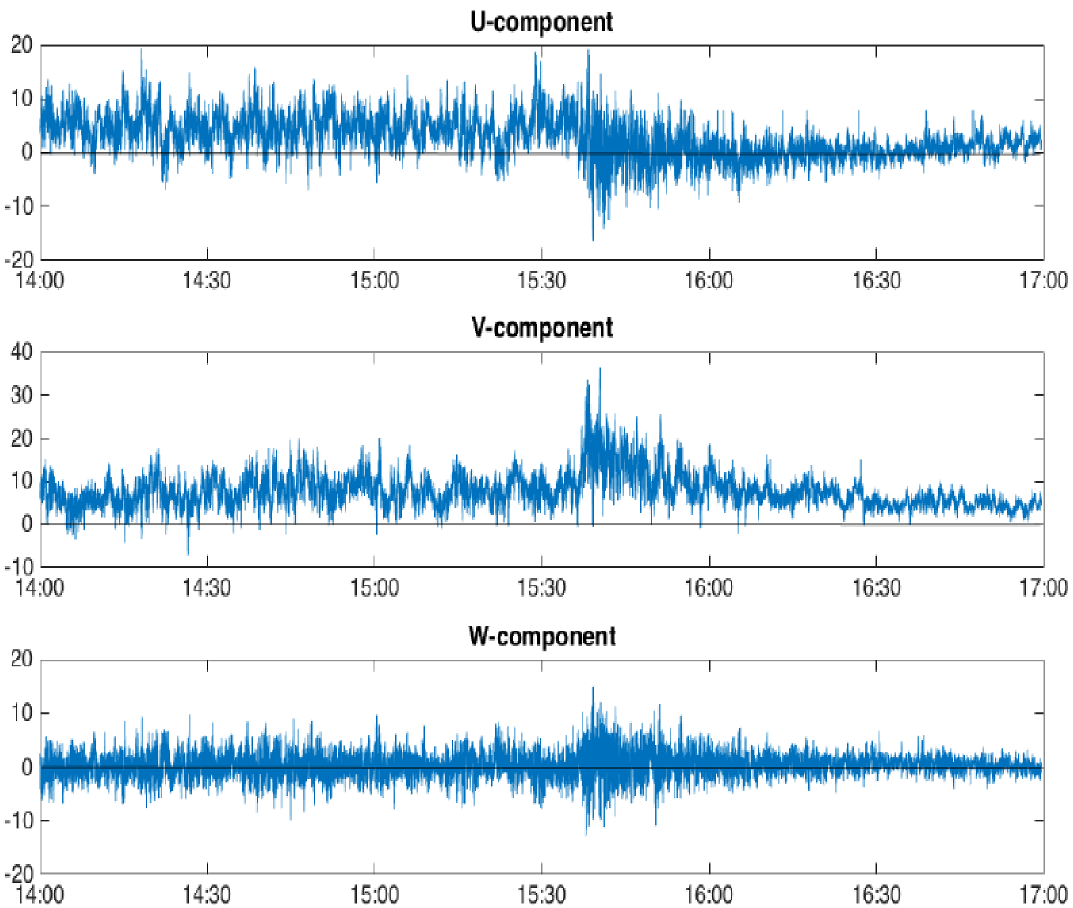

Fig. 1. Variations of the zonally (U) and meridionally (V) oriented components of the wind (m/s), as well as the vertical velocity (W) components during 3 hours (14-17) on 29.05.2017 from measurements at PF MSU.

Wavelet analysis revealed cyclic features in wind variations - with typical periods of about 40 minutes, 15-20 minutes and shorter-period variations (with a period about 4 minutes or less). A qualitative change in the spectral structure of the wind dynamics after a strongest squall of about 15:39 has been noted. In particular, after the squall there were no significant short-period wind fluctuations (with a period of several minutes). After the squall, relaxation oscillations for the wind were noted. Cross-wavelet analysis of mutual variations of different wind components revealed a significant change in their coherence after a strongest squall.

Figure 2 shows local coherence of U- and V-components for three hours (14-17) on 29.05.2017 from measurements at PF MSU. According to Fig. 1, a strong squall at 15.39 initiated a chain of coherent variations of the U and V wind speed components with increasing characteristic period. These variations are characterized by positive correlation. It should be noted the manifestation of significant coherence for variations of U and V components with periods about 20-30 minutes about an hour before the record squall in 15:39. These variations are characterized by negative correlation. Significant coherence of U and V variations with periods of about half an hour was manifested long enough (at least two hours). According to the results obtained, one can expect some possibilities of prognostic significance in assessing the risk of extreme squalls.

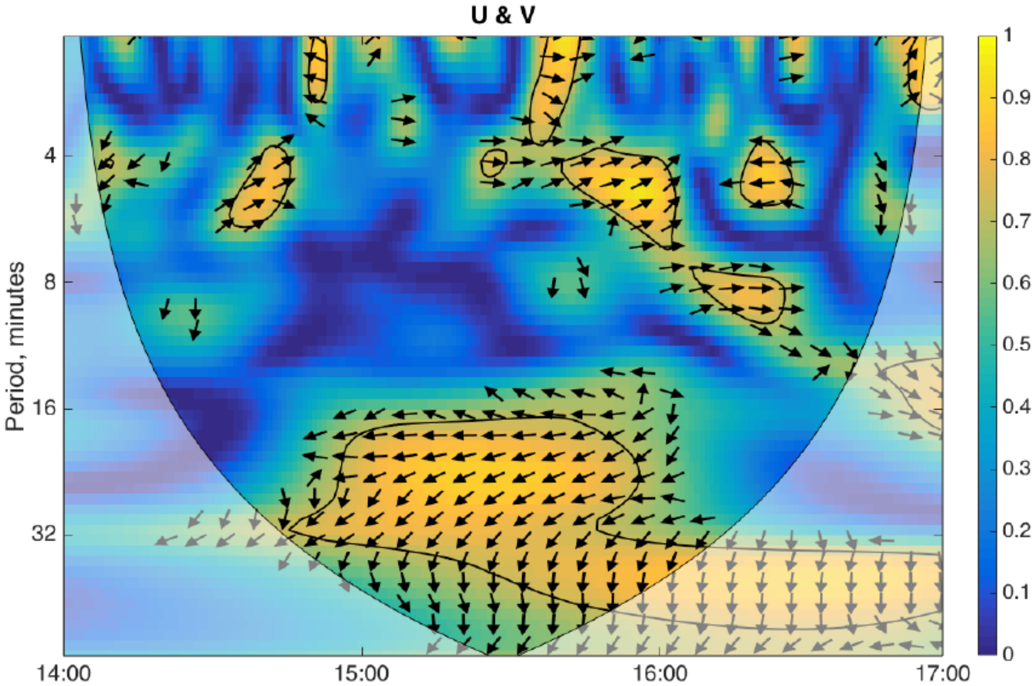

Fig. 2. Local coherence of U- and V-components for three hours (14-17) on 29.05.2017 from measurements at PF MSU.

Similar measurements were made on April 21, 2018, when during the strongest squall (at 17:04) a wind of hurricane strength was also registered. As in May 2017, the extreme wind in Moscow in April 2018 was associated with the atmospheric front. The strongest squalls marked in the spring of 2017 and 2018 are very unusual and rare in the Moscow region. The recurrence of such strong squalls within one year is unique.

Regional intraseasonal anomalies in transitional seasons in Northern Eurasia

Parfenova M.R.[1], Mokhov I.I.[1,2]

[1]A.M. Obukhov Institute of Atmospheric Physics RAS
[2]Lomonosov Moscow State University
parfenova@ifaran.ru

The number of hazardous meteorological phenomena in Russia is increasing by about 6-7% per year since the end of the 20th century, according to observations (http://www.meteorf.ru/). Last year (2017), this number was four times higher than it was in 2000, when very extreme spring with high temperature in March and cold air outbreaks in May in Russian regions were observed. Analysis of intraseasonal variability of surface air temperature (SAT) from long-term observations reveals multimodal features in probability density functions (PDF), in particular for transitional (spring, autumn) seasons (Agayan and Mokhov, 1989; Mokhov and Semenov, 1997; Mokhov et al., 1998; Mokhov, 2017). The PDF polymodality can be a result of various climatic processes. In (Mokhov and Semenov, 1997; Mokhov, 2017) the analysis of bimodal features of PDF for intra-seasonal SAT variations was performed, using a stochastic energy balance model and daily data from long-term (since the end of the 19th century) observations at various Eurasian meteorological stations. In particular, the formation of the PDF bimodality for regional SAT anomalies can be related to the nonlinear temperature dependence of surface albedo near the snow boundaries and meridional heat transfer.

We present here some estimates of the PDF polymodality for SAT anomalies and their changes in last decades from observations in Russian regions. Figures 1,2 show the frequency of different SAT anomalies near Lake Baikal (in Irkutsk) in spring and autumn for two decades (1956-1965 and 2006-2015). The Lake Baikal basin is characterized by strong thermal and hydrological anomalies during last years.

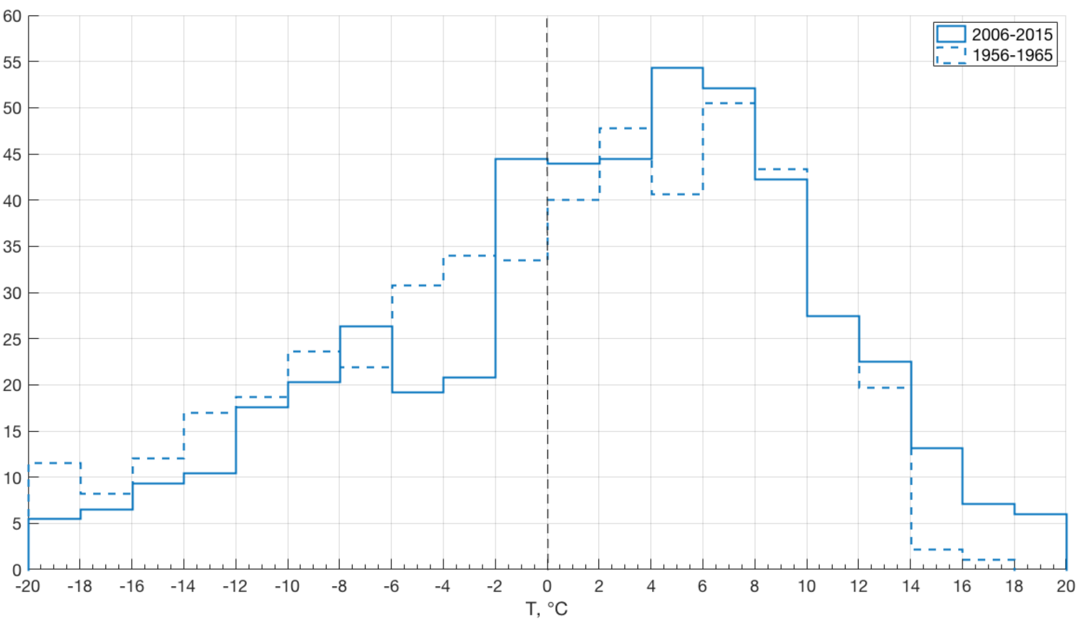

Fig. 1. Frequency (number of days) of different SAT anomalies in autumn in Irkutsk for two decades (1956-1965 and 2006-2015).

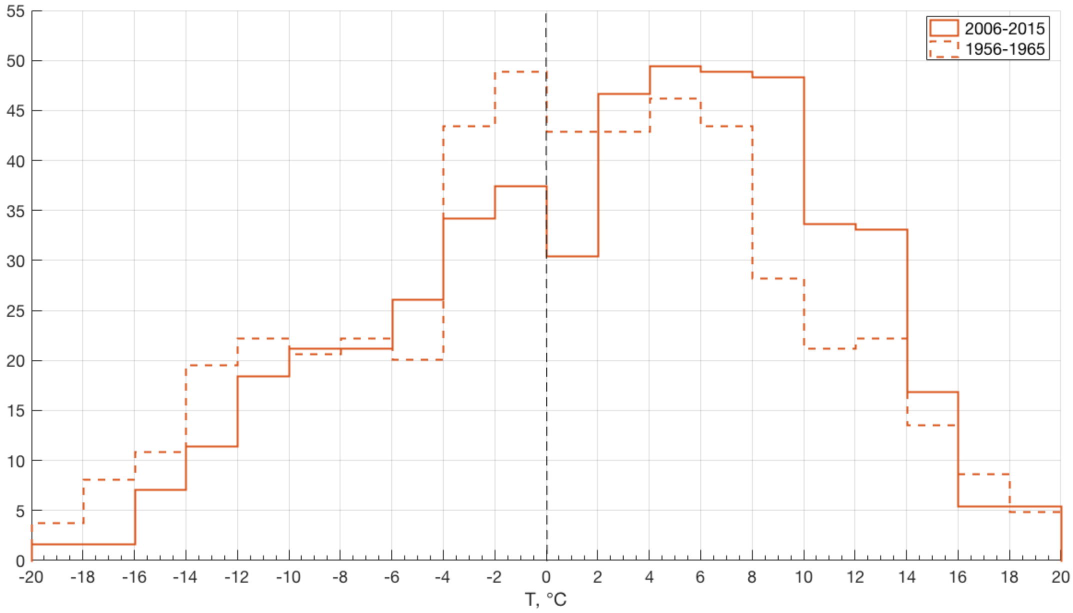

Fig. 2. Frequency (number of days) of different SAT anomalies in spring in Irkutsk for two decades (1956-1965 and 2006-2015).

Figures 1,2 display the polymodal (bimodal) features of the PDF for SAT anomalies in Irkutsk. It should be noted that general warming during last decades is accompanied by a more pronounced manifestation of bimodality near 0^{o}C, in particular in spring. Similar estimates were obtained for other North Eurasian regions, in particular for Moscow and Arctic and subarctic regions. For different regions, the changes in the distribution functions for SAT anomalies vary significantly. This is also due to the different times for transition of the temperature near surface through 0^{o}C.

This work was carried out within the framework of RFBR projects and RAS programs.

References

Agayan G.M. and I.I. Mokhov (1989) Quasistationary autumn atmospheric regimes of the Northern Hemisphere during the period of the FGGE. *Izvestiya, Atmos. Oceanic Phys.*, **25**, 851-855.

Mokhov I.I. (2017) Multiple climatic regimes in transitional seasons. *Research Activities in Atmospheric and Oceanic Modelling*. E. Astakhova (ed.). WCRP Rep. No.12/2017, 2.09–2.10.

Mokhov I.I. and V.A. Semenov (1997) Bimodality of the probability density functions of subseasonal variations in surface air temperature. *Izvestiya, Atmos. Oceanic Phys.*, **33**, 702-708.

Mokhov I.I., V.K. Petukhov and V.A. Semenov (1998) Multiple intraseasonal temperature regimes modelling of trends of the Earth's climate variability characteristics. *Izvestiya, Atmos. Oceanic Phys.*, **34**, 163-171.

Evaluation of Quality Control Methods and their influence on HYCOM model Background

Shastri Paturi[1], Ilya Rivin[1], Zulema Garraffo[1], Jim Cummings[1], Hae-Cheol Kim[1], Yan Hao[1] and Avichal Mehra[2]
[1]IMSG at NOAA/NWS/NCEP/EMC, [2]NOAA/NWS/NCEP/EMC
Email: Shastri.Paturi@noaa.gov; Phone: 301-683-3761

Observations are an integral part of any data assimilation system. Measured ocean observations are available from various sources, e.g., SST from satellites, SSH anomalies from altimeters, T&S from profiles, XBT's, moorings etc. Quality control (QC) of observations is required to make a decision on the validity of newly received data and requires information about the data. For profile observations the possible collocated products are climatology (e.g., GDEM), cross-validation (xval), analysis and forecast. The main purpose of the QC is to bring data validation information into the analysis process. While QC of observations is done at the data release time, real-time operational QC methods are also required to improve consistency of the data with simulated ocean states used in the data assimilation procedures (e.g., Navy Coupled Ocean Data Assimilation System – NCODA; Cummings and Smedstad, 2013). NCODA has a built-in QC that works in conjunction with its 3D variational algorithm (Cummings, 2011). At NCEP, 24-hr forecast fields are generated from the 1/12 deg global Real-Time Ocean Forecasting System (RTOFS). In this study, the influence of additional automated QC methods for real-time applications and the importance and consequences of using model background fields for QC in real-time operational ocean analysis and forecast is presented.

A few days of QC'ed profile data provided by the US Navy consisted of daily profile temperature (^{o}C) and salinity (psu) measured from Fixed Buoys, Drifting Buoys, Marine Mammals, Argo Floats, TESAC (Temperature, Salinity and Currents) and Expendable BTs. The QC'ed profile data was reformatted to obtain the pre-QC'ed incoming files. These files were input into the NCODA QC algorithm with the NCEP global HYCOM+CICE+NCODA (HYCOM; Bleck, 2002) generated forecast as background field.

The probability of error (E) for an observation w.r.t a background field can be computed from the normalized innovations as, I=(Obs-background)/σ, where σ is the error estimate of the background field. The error probability E that the observation contains a random error I is obtained from the normal distribution (Cummings, 2011). The US Navy profile data included xval information. The xval method computes corrections to climatology using observations against other nearby data. It is analogous to checking observations against a dynamic, time-dependent climatology. The error probability E for GDEM climatology and for the HYCOM 24-hr forecast was computed in addition to the error probability E for xval.

The total number of profiles available for March 01, 2017 are 7452 (Fig. 1), of which 2265 profiles have overall error probability values of less than 1.0 (Fig. 2a and Fig. 2b). The profile locations where HYCOM probabilities are smaller than climate are plotted in Fig. 2, indicating than HYCOM is a better predictor of profile temperature at ~68% of locations. The xval probabilities are also compared to the probabilities from GDEM in Fig. 3. The xval is found to be a better predictor of profile temperature than GDEM at ~44% of locations. However, in comparison to HYCOM, the profile locations where xval is a better predictor than GDEM climatology are more spread out. The profile temperature from three locations near equatorial Pacific are also compared to HYCOM and GDEM temperatures in Fig 3, where HYCOM is a better predictor of profile temperature than GDEM (blue circles: Fig 3 top panel) and GDEM is better predictor of profile temperature than HYCOM (red circles: Fig 3 top panel). Replacing GDEM climatology with HYCOM forecasts as background field would on average improve the QC of the profile data more than xval, but this occurs in regions where there is repetition in measurements (e.g., TAO/TRITON buoys; glider transects off the California coast; Mediterranean moorings; Japan Meteorological Agency's repeat hydrography, etc). Extended regions containing different sources of profile data, where error probability E for HYCOM is large, indicate regions with low forecast skills. The same analysis was repeated for March 10, 2017 with similar results. As an additional by-product, including the HYCOM forecast in the QC will give an indication of HYCOM forecast skill. This experiment is the first step in testing the use of including ocean forecasts to QC ocean observations and is being further investigated.

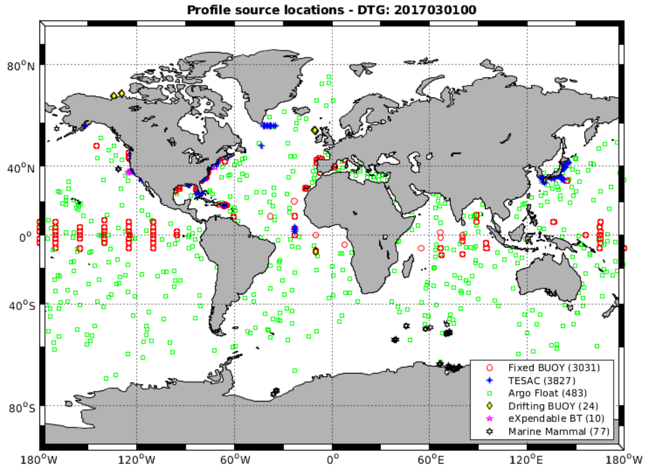

Figure 1. Locations of profile data – March 01, 2017.

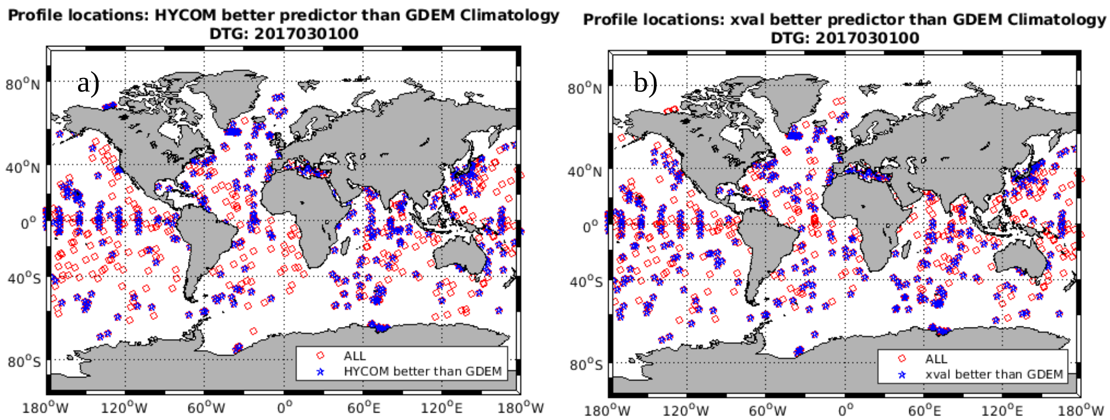

Fig 2. Locations of profiles where (a) HYCOM is a better predictor than GDEM and (b) xval is a better predictor than GDEM.

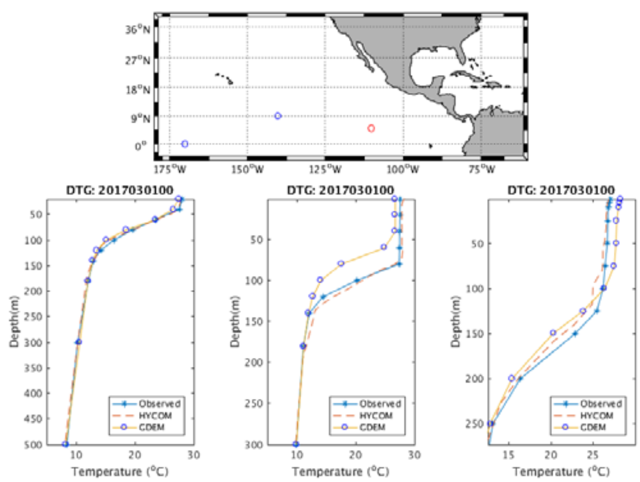

Figure 3. Profile Temperature comparison with HYCOM and GDEM climatology at three locations, where HYCOM is a better predictor of profile temperature than GDEM (blue circles-top panel) and GDEM is better predictor of profile temperature than HYCOM (red circle-top panel). Profile figures left to right correspond to profile locations from west to east.

Bleck, R. 2002: An oceanic general circulation model framed in hybrid Isopycnic-Cartesian coordinates, Ocean Modell, 37, 55-88.

Cummings, J. A. 2011: Ocean Data Quality Control, Operational Oceanography in the 21st Century, Chapter 4, 91-121.

Cummings, J.A. and O.M. Smedstad, 2013: Variational data assimilation for the global ocean. In: S.K. Park and L. Xu (Eds.), Data Assimilation for Atmospheric, Oceanic and Hydrologic Applications Vol. II., doi: 10.1007/978-3-642-35088-7_13, Springer-Verlag, Berlin Heidelberg.

Evolution and tracks of tropical cyclones in 2016 in the Pacific Ocean.

Pokhil A.E.

Hydrometcenter of Russia, 123242, Moscow, Bolshoy Predtechenskiy per. 9-11
e-mail: AEPokhil@yandex.ru

The evolution and motion of a series of tropical cyclones (TC) in 2016 in the Pacific Ocean are investigated in this work. Cases of triple interaction of TCs and the influence of a polar front (PF) on them are considered. The dynamics of groups of real tropical cyclones is compared with the behaviour of perfect cyclonic vortices in experiments with a numerical model. Variants of explanation of the origination of loops, zigzags and sharp turns in the cyclones tracks are suggested.

From August 19 a group of vortices constituted by three tropical cyclones – Tropical Storm (TS) Mindulle, TS Lionrock N10 and Tropical Depression (TD) Kompasu – moved synchronously on the Pacific Ocean north-eastern water area. The tracks of the TCs included sharp turns and loops (Fig.1a).

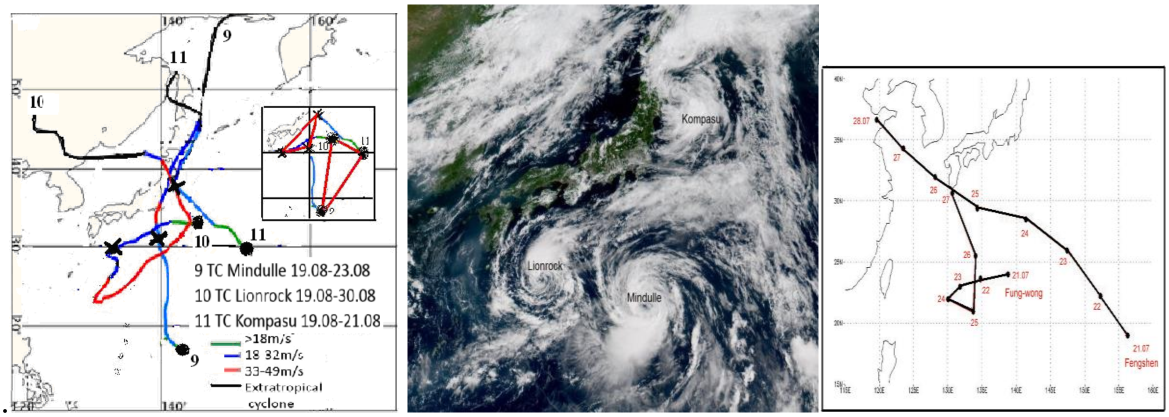

1a 1b 1c

Fig.1. a/ The tracks of TCs Mindulle, Lionrock, Kompasu from 19 to 30 August 2016. Black circles show the moments of the beginning of the interaction of cyclones, crosses show the moments of the end of their interaction. The inset shows some parts of the tropical cyclones during their interaction. It can be seen that the triangle between the three centers of the cyclones turned counterclockwise and is significantly smaller at the end of the cyclones interaction compared with such triangle in the beginning of their interaction. It bears evidence of strong interaction of the tropical cyclones;
1b/ satellite image of the cyclones Mindulle, Lionrock, Kompasu 2016-08-21 000Z (visible range). Cloud structures connecting the vortices are distinctly visible;
1c/ the trajectories of the TCs Fung Wong and Fengshen in July 2002.

In this area of the ocean such situations are observed rather often. One of such examples: the trajectory of the TC Fung Wong described a loop during its interaction with the TC Fengshen, which was similar to the loop of the TS Lionrock trajectory (Fig. 1c). A loop forms in the trajectory of a weak tropical cyclone under the influence of the circulation of a stronger vortex.

The interaction and rotation of the TCs under investigation in a cyclonic orbit lasts till the moment when a polar front (PF) approaches them from the north-west. Between August 20 18:00 and August 21 0 hours 2018 Kompasu settles on the PF that approached it well closely and, under its influence, sharply turns (almost a 90º turn) in the north-eastern direction (Fig. 1a). Then it merges with the PF and quickly moves in the north-eastern direction in the flow of PF.

Less than in 24 hours Mindulle also turns north-eastwards (on August 21, at 12:00) in the direction to closely approached PF, for some time it describes the trajectory of Kompasu that passed further (Fig. 1a) and, on August 22, approximately in 02:00, it also settles on the PF that approached it from the east side, and “tears up” it. Then Mindulle begins to move to the north-north-east direction at a great velocity following the steering flow, that is, the northern part of the PF.

A series of numerical experiments using a barotropic model of the atmosphere based on the “shallow water” equations was carried out. The investigation dealt with the behaviour of a group of perfect distributed vortices (in a rotating field) located in a way analogous to the location of real TCs. As a result of calculations the patterns of the evolution of the vorticity fields ($10^{-5}c^{-1}$) and the tracks of the interacting vortices were obtained (Fig. 2).

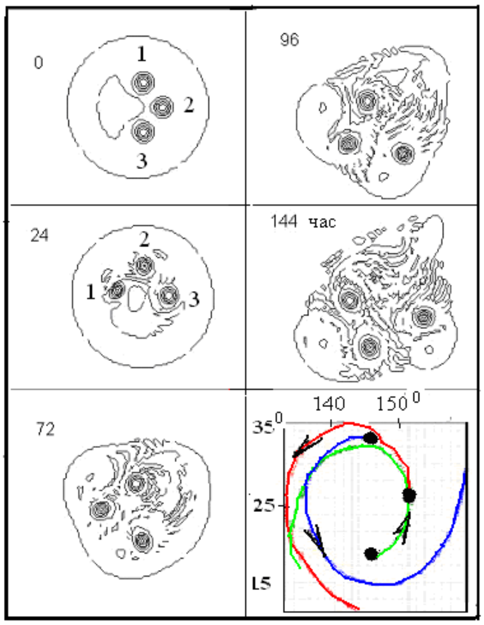

Fig. 2. Patterns of the evolution of the vorticity fields ($10^{-5}c^{-1}$) and tracks of the interacting vortices. The integration time is 144 hours.

Conclusions

1. The interaction of the vortices with one another and with other baric formations can lead to meandering and loop-like motion of these vortices.

2. Based on the experiments using a numerical model and the data from satellites the explanation of the motion of tropical cyclones under investigation is found. A numerical experiment with a group of three perfect distributed vortices substantiated the hypothesis about the cause of the loop-like motion of the TS Lionrock. The strange trajectory of Lionrock was successfully explained by its interaction with two TCs (Mindulle and Kompasu) which existed simultaneously with the first one.

3. On the basis of satellite data it was shown that the action of a polar front on the motion of the TCs Mindulle and Kompasu had interrupted the interaction between these TCs and the TS Lionrock.

Sectorial variations in the Antarctic circumpolar trough and inferences for the Ekman transport of sea ice

Ian Simmonds and Dominic Thorn

School of Earth Sciences, The University of Melbourne, Victoria 3010, Australia
simmonds@unimelb,edu.au

Since satellite records commenced in 1979 the total Antarctic sea ice extent has exhibited variability and trends (and reached a new annual-mean low record in 2017). We are exploring the extent to which the variability can be related to the large-scale SH atmospheric drivers and, in particular, the Semiannual Oscillation (SAO). This mode arises because the thermal inertia of the Southern Ocean and of the Antarctic continent are very different, and hence the cycle of atmospheric temperature in the midlatitudes differs from that at high latitudes. A consequence of this is that the mid- and high-latitude temperature difference exhibits a strong temporal wavenumber 2 over the year (the SAO). Hence there is strong SAO signal in baroclinicity and in the strength and location of the Circumpolar Trough (CPT) (van Loon 1967, Simmonds and Jones 1998, Walland and Simmonds 1999, Simmonds 2003, Simmonds and King 2004).

Fig. 1 shows the mean (1979-2017) annual cycle of the latitudes of the zonal-average sea ice edge and the CPT (from ERA-Interim). For summer and autumn the ice edge is poleward of the CPT, and hence the marginal ice zone (MIZ) is overlaid by easterlies. As a consequence, the Ekman ice transport is to the south, a factor which associated with sea ice extent (SIE) reduction. The opposite holds during winter and spring. Hence SIE variations are strongly influenced by the relative positioning of the CPT and MIZ (Watkins and Simmonds, 1998).

Fig. 2 displays plots analogous to that in Fig. 1, but for the averaged longitude sectors of 30-60^{o}E, 120-150^{o}E, 210-240^{o}E, and 300-330^{o}E. In contrast to the zonally-averaged case note that over 120-150^{o}E the ice is to the **south** of the trough in almost all months. The **opposite** is true for the 210-240^{o}E sector, meaning that the meridional Ekman forcing is in opposite directions in these two sectors throughout the year. Also note that the interannual range of sea ice implies that the direction of Ekman ice forcing in the MIZ for a given calendar month depends on the ice amount present.

References

Simmonds, I., 2003: Modes of atmospheric variability over the Southern Ocean. *J. Geophys. Res.*, **108**, 8078.

Simmonds, I., and D. A. Jones, 1998: The mean structure and temporal variability of the semiannual oscillation in the southern extratropics. *Int. J. Climatol.*, **18**, 473-504.

Simmonds, I., and J. C. King, 2004: Global and hemispheric climate variations affecting the Southern Ocean. *Antarc. Sci.*, **16**, 401-413.

van Loon, H., 1967: The half-yearly oscillations in middle and high southern latitudes and the coreless winter. *J. Atmos. Sci.*, **24**, 472-486.

Walland, D., and I. Simmonds, 1999: Baroclinicity, meridional temperature gradients, and the southern Semiannual Oscillation. *J. Climate*, **12**, 3376-3382.

Watkins, A. B., and I. Simmonds, 1998: Relationships between Antarctic sea-ice concentration, wind stress and temperature temporal variability, and their changes with distance from the coast. *Ann. Glaciol.*, **27**, 409-412.

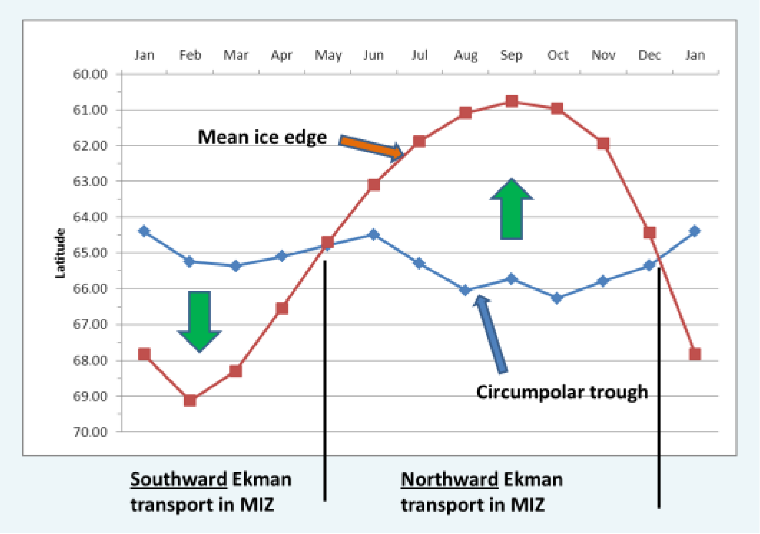

Fig. 1: Mean annual cycle of the latitudes of the zonal-average sea ice edge and the CPT.

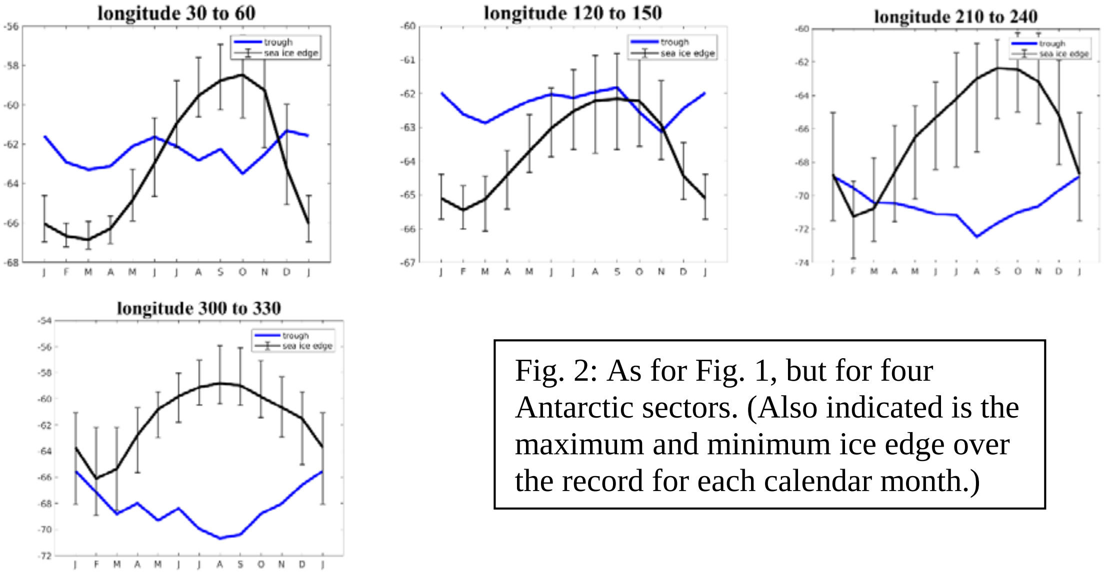

Fig. 2: As for Fig. 1, but for four Antarctic sectors. (Also indicated is the maximum and minimum ice edge over the record for each calendar month.)

Distribution features of travelling eddies in the South China Sea

Meng Zhang, Hans von Storch

Institute for Coastal Research, Helmholtz Zentrum Geesthacht, Geesthacht, Germany

By means of a 0.1-degree daily ocean simulation STORM (supported by the German consortium project STORM; J. von Storch et al, 2012), this paper has investigated the characteristics of the travelling eddies in the South China Sea (SCS) from 1950 to 2010 using daily data. The STORM dataset, forced by the 6-hourly NCEP reanalysis data, realistically capture the hydrodynamics in the SCS (Zhang and H. von Storch, 2017). Based on a monotonicity-based eddy detection and tracking method, eddies in the SCS have been detected and tracked from the gridded sea surface height anomaly (SSHA) field of STORM (Zhang et al, 2017). In this paper, we focus on eddies with high relative intensity and long travel length. They fulfill the following criteria:

1. The accumulated travel length is 100 km or more, and the ending point is required to be at least 50km away from the beginning one.
2. All the eddy points must have relative intensity (RI) over 3 mm. In addition, the RI of the strongest point along one track surpasses 6 mm. RI is defined by the absolute difference between the extremum SSHA and the averaged SSHA of its 24 neighbors.
3. An eddy track must travel for over 90% of its lifetime in water deeper than 200 m, which allows the eddy to extend in the vertical direction.

From 1950 to 2010, a total of 1871 anti-cyclonic eddies (AE) and 4219 cyclonic eddies (CEs) were detected, corresponding to 65137 AE points **(2.9 per day)** and 143798 CE points **(6.5 per day)**. We extracted the time series of the daily eddy number, and plotted the distribution probability (Fig. 1) of daily AE points and daily CE points. **Daily AE number varies from 0 to 9, with the most frequent number of 3, and daily CE number ranges from 0 to 17, with the most frequent number of 6.**

The maximum of 9 AEs appears once in 12 continuous days, which are 09 – 20/05/1981. And the maximum of 17 CEs occur once in 3 days of 21 – 23/03/2005. As an example, the eddies occurring in 09/05/1981 and in 21/03/2005 are all collected in Fig. 2. **Most of the AEs are located along the SCS western coast and near the Luzon Strait, except some CEs in the Sulu Sea. And when the maximum number of one type eddy takes place in one day, many of the other type eddy occur as well.**

von Storch, J.-S., C. Eden, I. Fast, H. Haak, D. Hernández-Deckers, E. Maier-Reimer, J. Marotzke, and D. Stammer (2012), An estimate of the Lorenz energy cycle for the world ocean based on the STORM/NCEP simulation, Journal of physical oceanography, 42(12), 2185-2205, doi: http://dx.doi.org/10.1175/JPO-D-12-079.1.

Zhang, M., and H. von Storch (2017), Toward downscaling oceanic hydrodynamics–suitability of a high-resolution OGCM for describing regional ocean variability in the South China Sea, Oceanologia, 59(2), 166-176, doi: 10.1016/j.oceano.2017.01.001.

Zhang, M., H. von Storch, and D. Li (2017), The effect of different criteria on tracking eddy in the South China Sea, Research Activities in Atmospheric and Oceanic Modelling (WGNE Blue Book), 2.25.

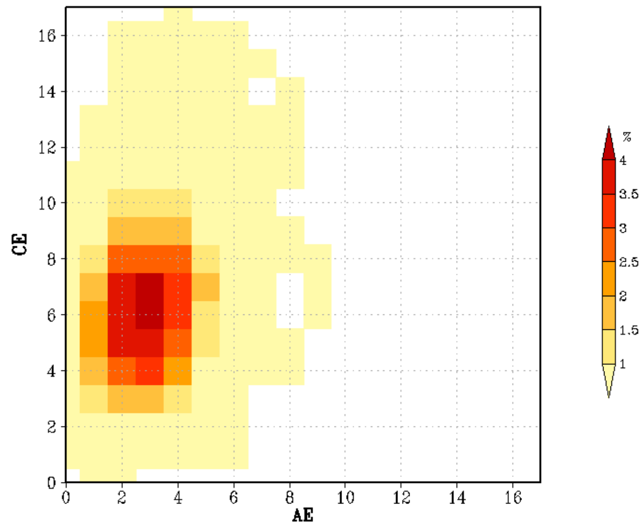

Figure 1. The occurrence probability of daily AE number and daily CE number.

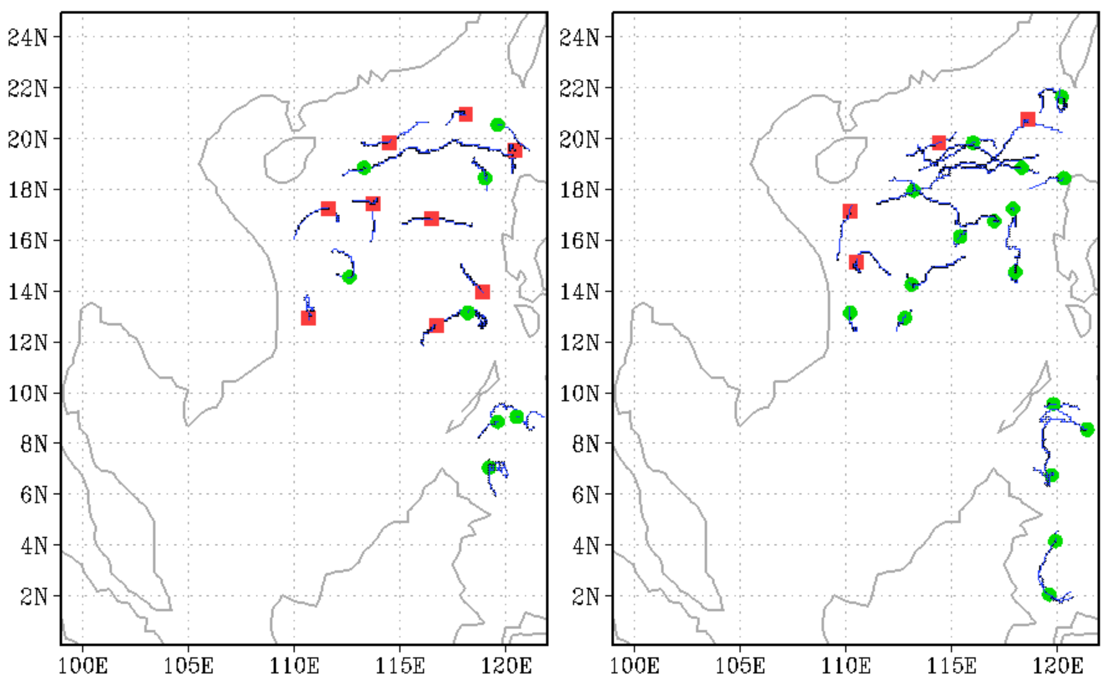

Figure 2. The tracks that appeared in 1981/05/09 (the left figure) and 2005/03/21 (the right one); Red squares and green circles present AEs and CEs at certain date.